RESERVOIR CHARACTERIZATION OF THE HARTSELLE SANDSTONE IN THE VICINITY OF GORGAS POWER PLANT, USING AMPLITUDE VARIATION WITH OFFSET (AVO)

by

THU ANH NGUYEN

ANDREW M. GOODLIFFE, COMMITTEE CHAIR
SAMANTHA E. HANSEN
JACK C. PASHIN
BO ZHANG

A THESIS

Submitted in partial fulfillment of the requirements
for the degree of Master of Science
in the Department of Geological Sciences
in the Graduate School of
The University of Alabama

TUSCALOOSA, ALABAMA

2018

ABSTRACT

The Black Warrior Basin (BWB) contains prolific oil and gas reservoirs, which have been well characterized to the west of two major coal-fired power plants in Alabama. The Mississippian Hartselle Sandstone of the BWB is a major oil sand resource in the United States. A stratigraphic test well, drilled at the William C. Gorgas Power Plant, Walker County, Alabama, revealed light crude oil (40°API) in the Hartselle Sandstone at 2,601.3 ft. (792.9 m) below ground surface. Two 5-mile, 2-D Vibroseis seismic reflection lines, which intersect near the stratigraphic test well, exhibit classic amplitude variation with offset (AVO) responses along the Hartselle Sandstone unit. Using an AVO intercept-gradient analysis along the target horizon (Hartselle Sandstone) across the seismic reflection profiles, the lateral extent of the hydrocarbon resource was mapped up to 1.3 km (0.8 miles) from the test well. The Hartselle Sandstone in the Gorgas area is considered a tight oil sand prospect and is higher impedance than the overlying limestone. The AVO analysis results show a pattern of positive amplitude decreasing with larger offsets consistent with a class I AVO anomaly, typical of high impedance hydrocarbon-saturated sands. The hydrocarbon zone within the Hartselle Sandstone extends a distance of 594 m (1948.82 ft) along line 101 and a distance of 1284 m (4212.60 ft) along line 201. These distances were used to estimate the areal extent of the hydrocarbons along each seismic reflection line, which averages 0.2 km^2 (50 acres) for line 101and 0.5 km^2 (146 acres) for line 201. In addition to this areal extent estimation, volumetric and risking analysis indicates that the Hartselle

Sandstone in the Gorgas area has a large resource potential, with an estimated total volume of hydrocarbons in place ranging from 0.1 to 5.6 million barrels of oil.

DEDICATION

I want to dedicate this work to my parents and my husband who have been supporting me all the way.

LIST OF ABBREVIATIONS AND SYMBOLS

s Seconds

ms Milliseconds

m Meters

km Kilometers

ft Feet

twt Two-way time

owt One-way time

AVO Amplitude Variation with Offset

BWB Black Warrior basin

CDP Common depth point

CMP Common mid-point

Hz Hertz

Mmbo Million barrels of oil

NMO Normal moveout

V_p P-wave velocity

V_s	S-wave velocity
=	Equal to
%	Percent
θ	Theta - Angle

ACKNOWLEDGEMENTS

A special thanks to Dr. Andrew M. Goodliffe, my thesis advisor, for his expertise, patience, guidance, and countless hours of helping me improve throughout the course of this research. I also want to thank my committee members, Dr. Samantha Hansen, Dr. Jack Pashin, and Dr. Bo Zhang for their expertise and helpful constructive criticisms. Thank you for agreeing to serve on my committee.

Thank you to the Department of Geological Sciences for allowing me to conduct my research and for providing the funding and assistance needed. Thank you for giving me the opportunity to teach the Geology 101 labs. Thank you to Marcella McIntyre-Redden and the Geological Survey of Alabama for allowing me to see the core samples and take photos of them for my research. Thank you to my colleagues, Berg Nazlim, Claudia Rubio Zapata, and Kalyn Tew for their support and sharing their knowledge.

Finally, I want to thank my family and friends. Special gratitude goes to my husband, Kyle Olsen, who inspired and encouraged me every single day. I am grateful for my grandparents, my parents, my parents-in law, and my siblings for their endless love and support.

CONTENTS

LIST OF TABLES

LIST OF FIGURES

CHAPTER 1: INTRODUCTION

1.1 Previous work and Motivation

To support a study of potential CO_2 storage from coal-fired power plants in the Black Warrior Basin (BWB), a stratigraphic test well, Gorgas #1, was drilled by The University of Alabama at the Gorgas Power Plant to a depth of 1,498 m (4,915 ft). Analysis of fluorescence and fluid saturations in the Gorgas #1 borehole indicate light crude oil (API gravity on the order of 40°), with saturation as high as 65.8% in the Mississippian Hartselle Sandstone (Figures 1.1-1.3; Clark et al., 2013). The amount of oil in place has been estimated to be 9,000 barrels per acre, or 360,000 barrels per 40-acre tract of land (Clark et al., 2013). Conventional core analysis results show that the Hartselle Sandstone has low porosity and contains many open natural fractures, indicating a tight oil prospect (Clark et al., 2013). However, the lateral extent of this oil resource is unknown. A 2-D Vibroseis seismic reflection survey was performed along two 8.05 km (5 miles) lines near the Gorgas Power Plant (Figure 1.4). Evidence of Amplitude Variation with Offset (AVO) anomalies was observed in the 2-D pre-stack seismic reflection data. In this study, an AVO analysis was conducted using the pre-stack versions of the seismic reflection data as well as well log data to evaluate the lateral extent of hydrocarbons in the Hartselle Sandstone within the area of the seismic reflection survey.

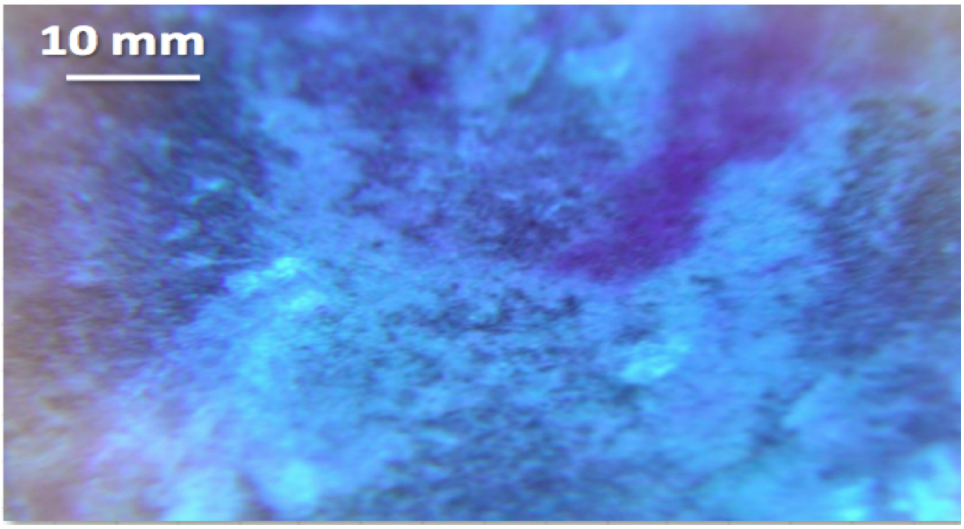

Figure 1.1. A flouroscope image of a Hartselle Sandstone core sample from a depth of 2675 ft from Clark et al. (2013). Dark coloration is the signature of pyrobitumen. Blue to white fluorescence indicates light crude oil with API gravity on the order of 40°.

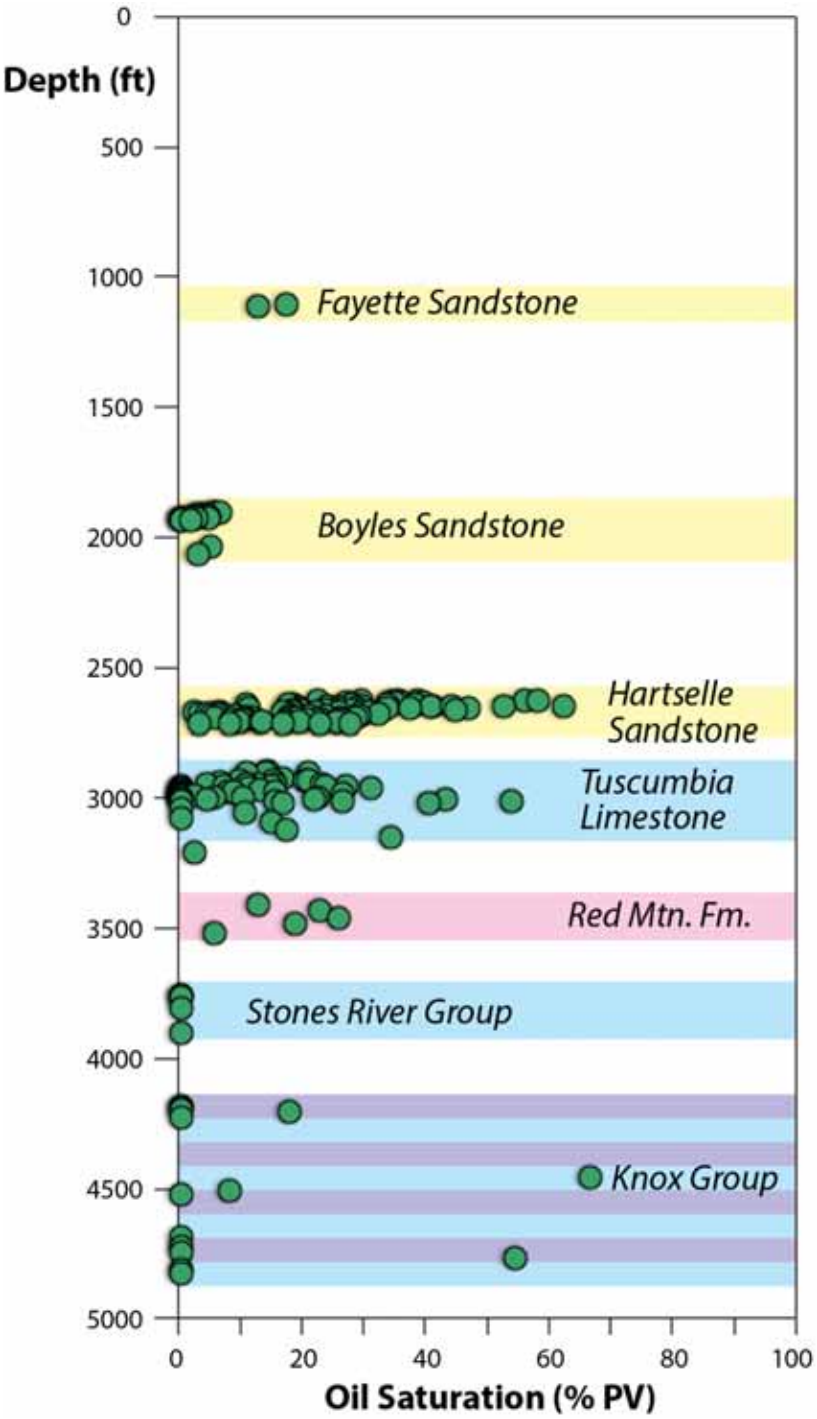

Figure 1.2. Oil saturation of the Gorgas #1 borehole plotted with depth (from Clark et al., 2013). Oil saturation within the Hartselle Sandstone is as high as 65.8%.

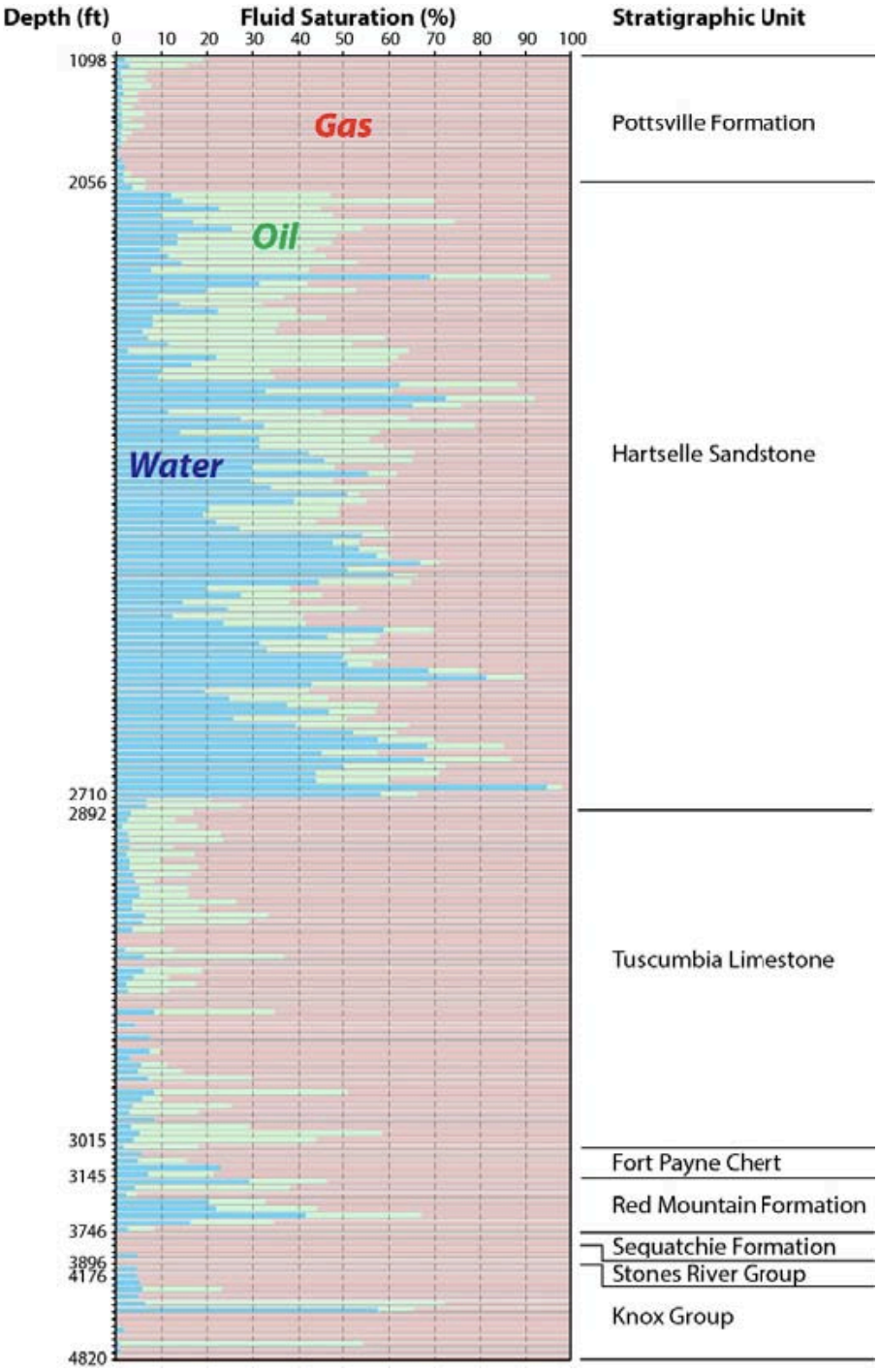

Figure 1.3. Chart showing the variability of fluid saturation versus reservoir depth in the Gorgas #1 borehole. (From Clark et al., 2013).

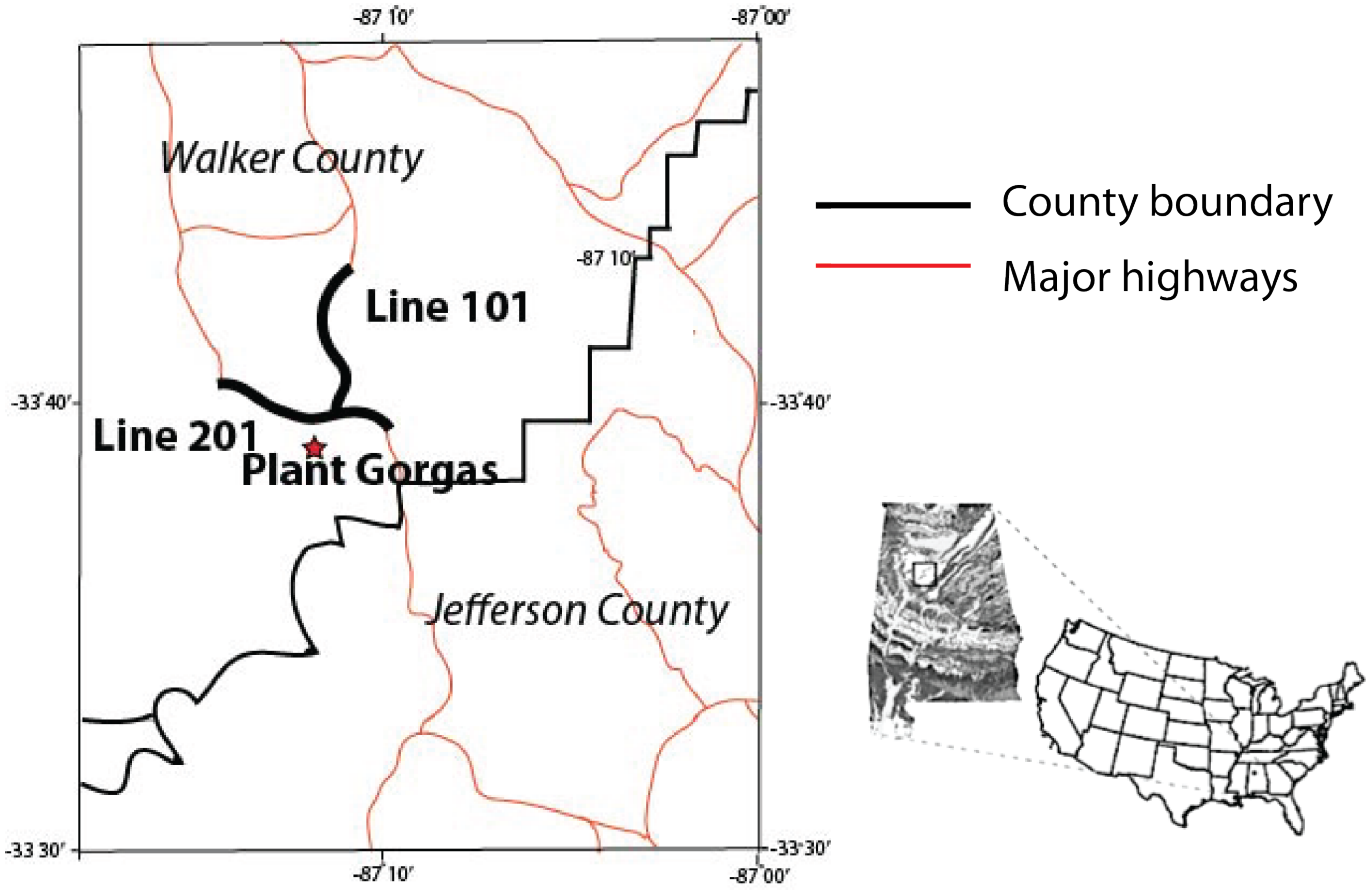

Figure 1.4. Map showing the locations of the seismic reflection lines from the 2-D survey near Gorgas Power Plant, Walker County, Alabama (modified from Rutter, 2012). Thick black lines, labeled line 101 and line 201, mark the seismic reflection profiles.

CHAPTER 2: GEOLOGIC BACKGROUND

2.1 Tectonics

The Late Paleozoic BWB extends from north-central Alabama to north-central Mississippi in the Alabama recess of the Appalachian and Ouachita orogenic belts (Figure 2.1; Thomas, 1985; Groshong, 2009). The basin covers an area of about 59,000 km^2 (23,000 $miles^2$; Ryder, 1987; Figure 2.1). Formed due to tectonic loading, the BWB is a peripheral foreland basin related to Ouachita and Appalachian orogenesis (Thomas, 1988). This triangular-shaped basin contains numerous northwest-trending, thin-skinned and basement-involved normal faults and is bounded by the Nashville Dome to the north, the Appalachian fold-thrust belt to the southeast, and the Ouachita fold-thrust belt to the southwest (Groshong et al., 2009). Most of the BWB faults follow the trend of the Ouachita thrust front. Formed in the Late Mississippian and developed primarily in the Pennsylvanian, the basin is a homocline that dips on average 2° southwestward beneath the Ouachita thrust (Thomas, 1988; Thomas and Whiting, 1994).

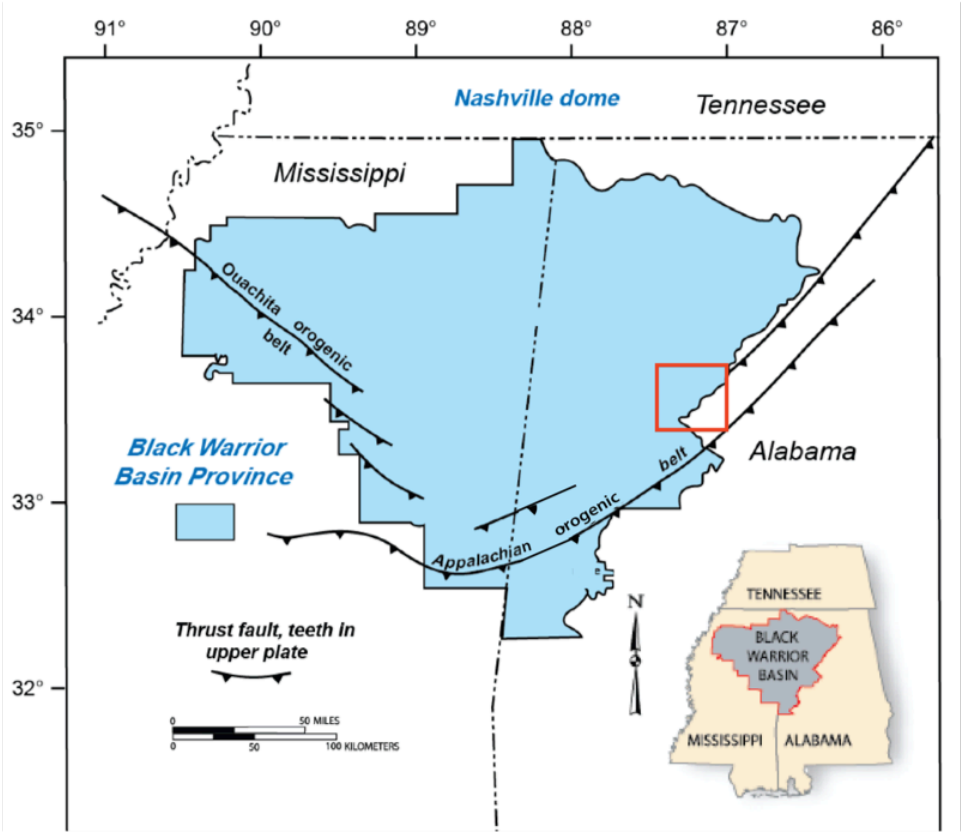

Figure 2.1. Tectonic setting of the BWB (blue shaded region; modified from Pawlewicz and Hatch, 2007). The red box indicates the location of the study area.

The tectonic history and stratigraphy (Figure 2.2) of the BWB can be briefly described as follows:

1) Late Precambrian – Early Cambrian: Iapetan rifting is indicated by transform faults along the Alabama-Oklahoma transform, the southern margin of the Alabama promontory, and extensional faults in the Birmingham graben and Mississippi Valley system (Robinson et al., 2012).

2) Middle Cambrian – Mississippian: A passive continental margin formed as recorded

by stable shelf carbonate facies (Robinson et al., 2012). The oldest Cambrian sedimentary rocks were deposited unconformably on Precambrian igneous basement rocks (Groshong et al., 2010). The oldest stratigraphic unit found in the Gorgas #1 well (Figure 2.2) is the Middle to Late Cambrian Conasauga Formation, which consists of fine-grained clastic and carbonate rocks (Rutter, 2012). The overlying Cambrian-Ordovician Knox group is composed of limestone and dolostone, representing a time of maximum transgression (Rutter, 2012). The Middle Ordovician Stone River Group and the Upper Ordovician Sequatchie consist of highly variable lithologies, including interbedded shale and limestone, and represent varying tidal environments on a carbonate shelf (Rutter, 2012). The Silurian Red Mountain Formation contains a heterogeneous succession of mudstone, sandstone, and limestone, where the base of the formation is identified by an oolitic ironstone (Thomas, 2007; Rutter, 2012). The Devonian Chattanooga shale is widespread throughout the basin (Pashin et al., 2010; Rutter, 2012). Both the Silurian Red Mountain Formation and the Devonian Chattanooga Shale are synorogenic deposits shed from the east during the Taconic and Acadian orogenic events (Rutter, 2012). The Lower Mississippian Fort Payne consists of siliceous micrite and bluish-gray nodular chert that has a gradational contact with the overlying Tuscumbia Limestone (Rutter, 2012).

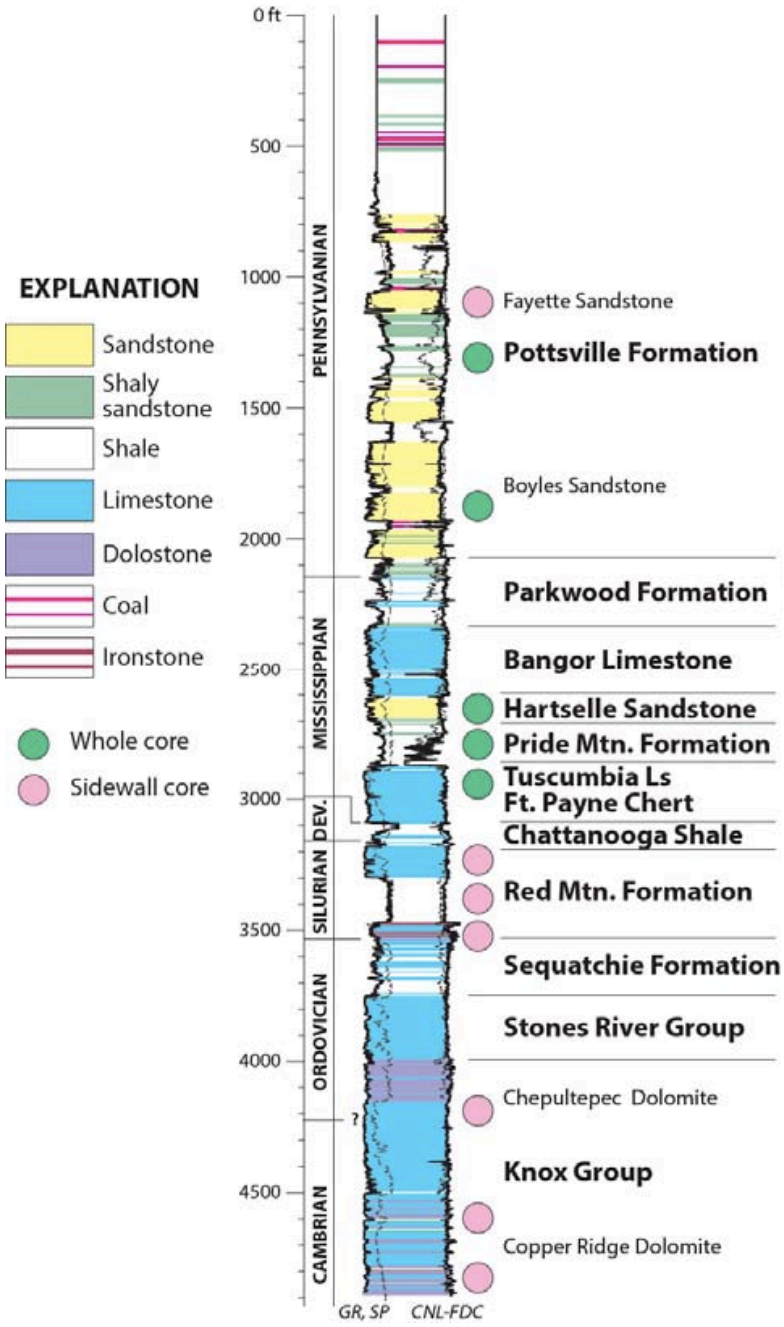

Figure 2.2. Stratigraphic column and well logs from the Gorgas #1 borehole from Clark et al. (2013), showing the major formations of the Black Warrior Basin.

3) Late Mississippian – Late Pennsylvanian: Ouachita orogenesis and Appalachian orogenesis began. The BWB stratigraphy shows that the Mississippian-Pennsylvanian units consist of a clastic wedge of deltaic, barrier, and shallow-marine sedimentary rocks (Figure 2.2; Thomas, 1985; Groshong, 2009). These units constitute the synorogenic basin fill during

Appalachian-Ouachita orogenesis, which consists of the Pride Mountain Formation, the Hartselle Sandstone, the Bangor Limestone, and the Parkwood Formation (Thomas, 1974). The Pride Mountain Formation is a heterogeneous unit composed of shale, limestone, and quartz arenite sandstone (Rutter, 2012). The Late Mississippian Bangor limestone, composed of a medium to dark grayish-tan limestone, was deposited on a carbonate platform (Rutter, 2012). The Pride Mountain-Parkwood strata contain a mixed carbonate-siliciclastic clastic and several hydrocarbons reservoirs, including the Lewis Sandstone (Pride Mountain), the Hartselle Sandstone, Carter Sandstone (Parkwood), Gilmer Sandstone (Parkwood), and Coats Sandstone (Parkwood) (Clark et al., 2013). The youngest stratigraphic unit in the basin is the early Pennsylvanian Pottsville Formation, which contains shale, sandstone, and economic coal seams. The Pottsville has been interpreted as a cyclic, fluvial-deltaic clastic wedge shed from the Appalachian orogenic belt (Pashin and Raymond, 2004).

4) Late Pennsylvanian – Mesozoic: The opening of the Gulf of Mexico is indicated by the northwest-trending system of normal faults that cut Paleozoic rocks within the BWB (Thomas, 1988). Triassic-Jurassic clastic rocks, evaporites, and volcanic rocks fill downthrown fault blocks (Thomas, 1988). Due to post-rift onlap, Cretaceous strata unconformably overlie the Paleozoic rocks in the western part of the BWB (Thomas, 1988).

2.2 Hartselle Sandstone

The focus of this study is the Hartselle Sandstone. Formed as a series of southwest-northeast trending barrier island and offshore bar complexes, the Hartselle Sandstone was deposited on a shallow and tide-dominated shelf (Thomas and Mack, 1982; Wilson, 1987). Mississippian sequence stratigraphy shows that in northwestern Alabama, the Hartselle Sandstone represents a terminal phase of a low-stand system tract, whereas in north-central

Alabama, the Hartselle Sandstone transitions into a transgressive system tract (Cleaves and Stapor, 1992). The Hartselle Sandstone was deposited between the Bangor Limestone to the northeast and the Floyd Shale to the southwest, mainly in the northeastern part of the BWB (Figure 2.3; Pashin,1994).

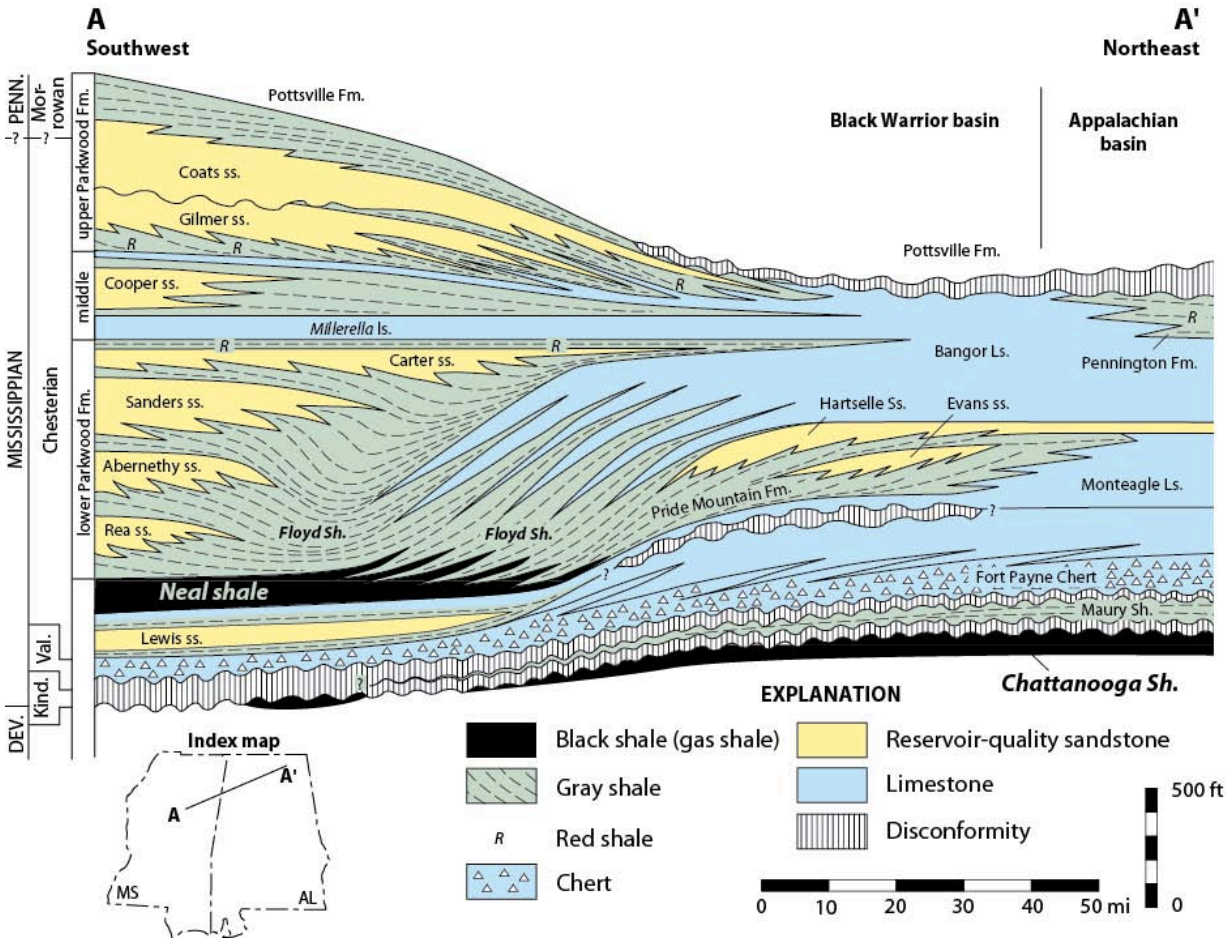

Figure 2.3. Generalized Mississippian stratigraphy of the BWB along a transect from northeastern Alabama to central Mississippi from Pashin (1994).

Up to 128.74 km (80 miles) wide and no more than 49 m (160 ft) thick, the Hartselle Sandstone is not only the thickest sandstone formation in the BWB but it also has the greatest areal extent of all the other sandstones of the Mississippian sequence (Wilson, 1987; Stapor and Cleaves, 1992). The outcrop belt of the Hartselle Sandstone is generally less than 8 km (5 miles) wide (Wilson, 1987). Figure 2.4 shows the extent of the Hartselle Sandstone in both outcrop and the

subsurface in northern Alabama. From north to south, the Hartselle Sandstone transitions from outcrop into the subsurface (Figure 2.4; Hills et al., 2016).

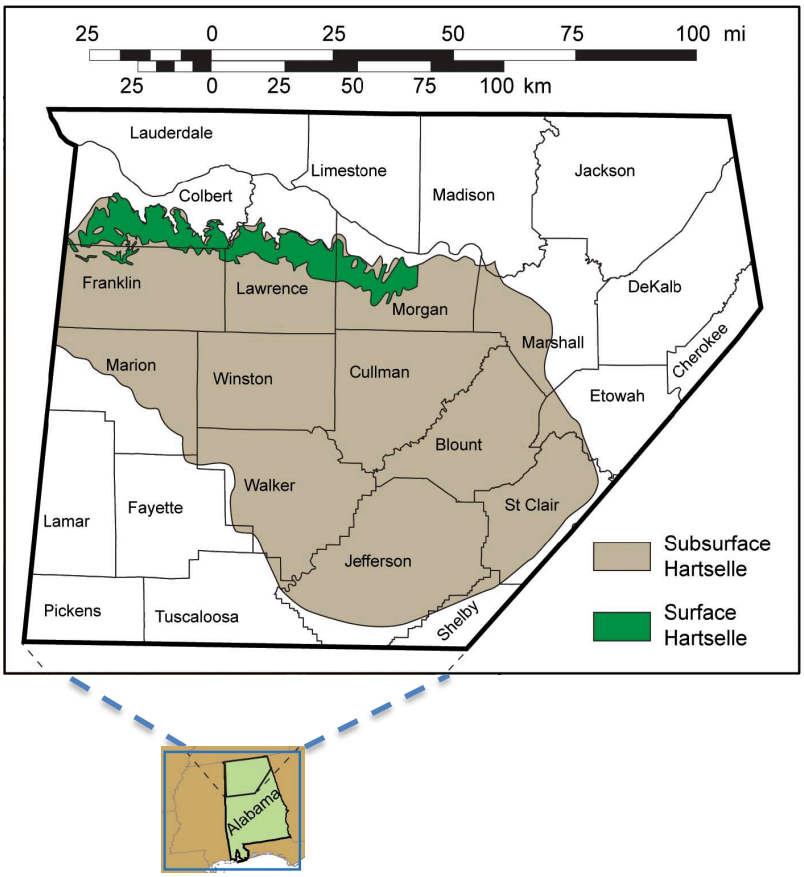

Figure 2.4. Map showing the extent of the Hartselle Sandstone in the subsurface (brown) and in outcrop (green) in northern Alabama. Adapted from Hills et al. (2016).

The Hartselle Sandstone is composed of fine-grained quartzose sandstone with a wide variation in porosity, permeability, bitumen saturation, and thicknesses of impregnated intervals (Wilson, 1987). Mississippian strandplain deposits generally have porosity of 6-19% and permeabilities ranging from 26 mD to as high as 663 mD (Rutter, 2012; Clark et al. 2013). Bituminous rocks or oil sands that are saturated with bitumen are exposed in outcrop at various locations from central Morgan County to Colbert County in north-central and northwest Alabama (Figure 2.5; Wilson, 1987; Hills et al., 2016). There are multiple probable source

formations for the bitumen in the Hartselle Sandstone. Those formations include dark-colored shales of the Mississippian Pride Mountain, Floyd Shale formations, and the Devonian Chattanooga Formation (Hills et. al., 2016). The average total organic carbon values of the Floyd and Chattanooga shales are greater than 2.0% and consist primarily of type II kerogen, which is rich in marine material and considered to be oil prone (Carroll et al., 1995). Although there has been no commercial exploration of these resources in Alabama, the potential of the Hartselle Sandstone could be significant (Hill et al., 2016).

Figure 2.5. Hartselle Sandstone outcrop showing bitumen seeping along a horizontal bedding plane from Hooks et al. (2016).

In the Gorgas #1 borehole, the Hartselle Sandstone, 26 m (86 ft) thick, is encountered at depths from 797 m (2615 ft) to 823 m (2702 ft) (Figure 2.2). At depths from 797 m (2615 ft) to 833 m (2733 ft), which includes the upper part of the Pride Mountain formation and the Hartselle Sandstone, was cored to determine the reservoir properties (Clark et al., 2013). A graphical core log of the upper Pride Mountain Formation and the Hartselle Sandstone in the Gorgas #1 borehole provides lithological and structural details of the Hartselle Sandstone core (Figure 2.6;

Clark et al., 2013). In the core, the Hartselle Sandstone is comprised of primarily very fine to fine-grained sandstone stained yellow-brown to brown with oil and in places black with pyrobitumen (Clark et al., 2013). It also contains abundant natural fractures (Figure 2.7; Clark et al., 2013). The Pride Mountain-Hartselle Sandstone interval displays an overall coarsening-upward sequence, suggesting progradational sedimentation (Figure 2.6; Clark et al., 2013). Sedimentary structures including current ripples, horizontal laminae, and shale intraclasts, were observed in several parts of the section, while cross-bedding was observed only in the upper 9.1 m (30 ft) of the core (Clark et al., 2013). Bioturbation occurs between 807.4 m (2649 ft) and 906.1 m (2645 ft) and concretionary carbonate sediment was found between 802.5 m (2633 ft) and 806.2 m (2645 ft; Clark et al., 2013).

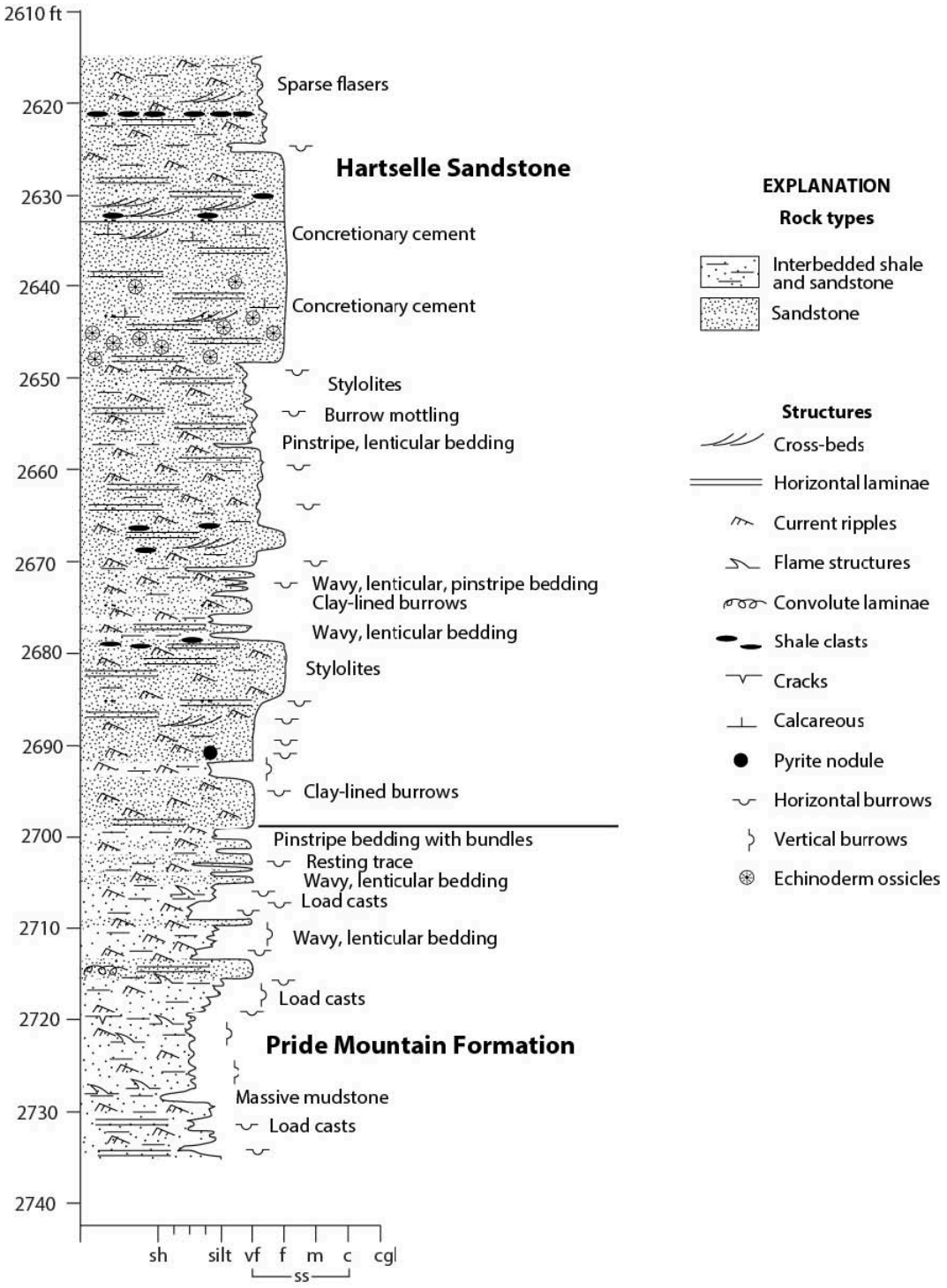

Figure 2.6. Graphic core log of the Pride Mountain Formation and Hartselle Sandstone in the Gorgas #1 borehole from Clark et al. (2013).

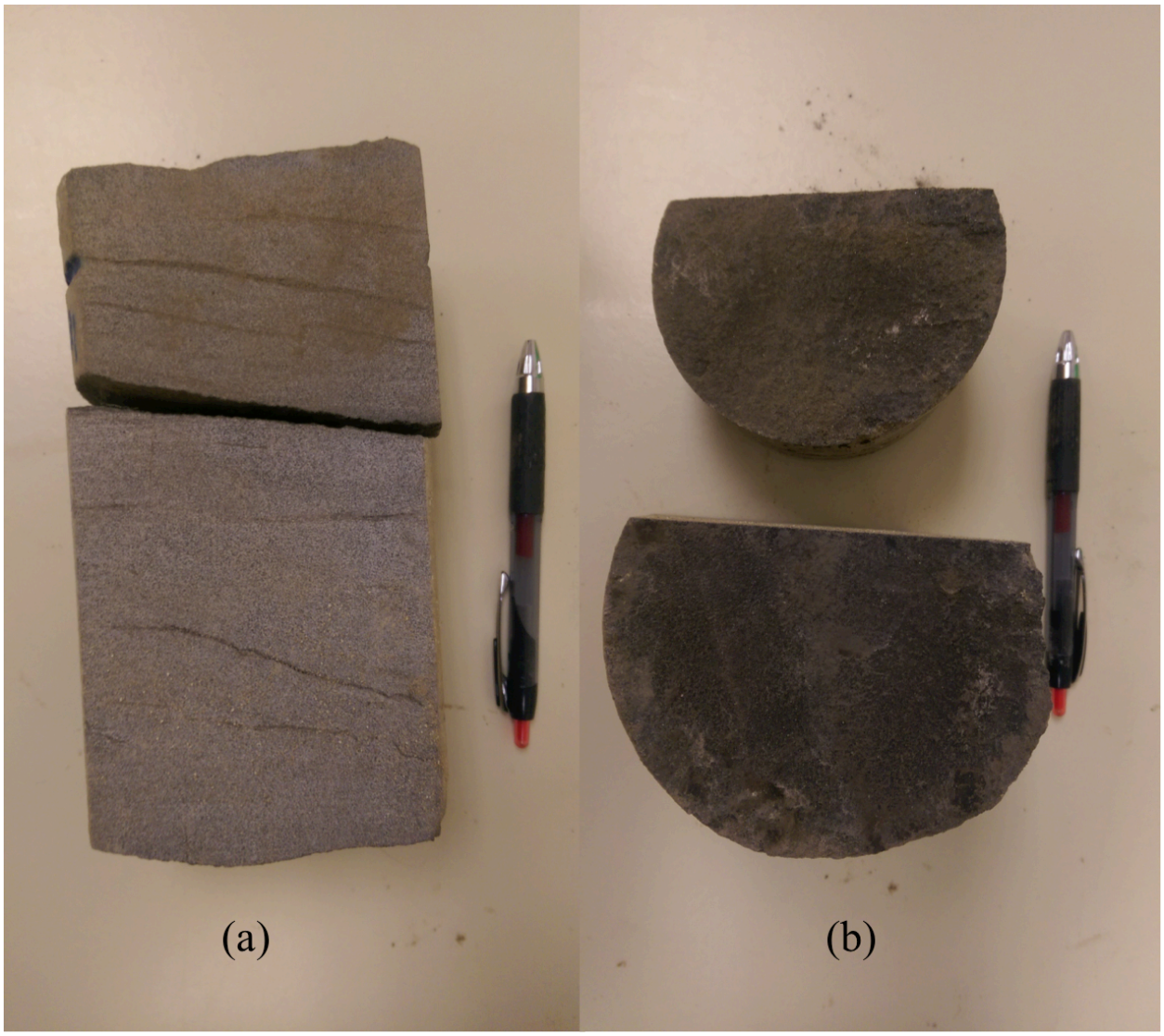

Figure 2.7. (a) Photo of the Hartselle Sandstone core, containing light yellowish oil stains and natural fractures. (b) Photo of the top of the Hartselle Sandstone core containing black pyrobitumen.

Based on the results of conventional core analysis (Clark et al., 2013), the porosity of the Hartselle Sandstone ranges from 0.5 to 8.3%. The average porosity in the Hartselle Sandstone is 5.2% with a standard deviation of 1.9. Permeability in the Hartselle Sandstone ranges approximately from 1000 mD to less than 0.001 mD, with an average value of 0.54 mD (Figure 2.8; Clark et al., 2013). The core analysis also evaluated the impact of natural fractures on

reservoir properties and shows that samples containing abundant natural fractures also have elevated permeability. Virtually all of the sample with permeability higher than 1 mD contain natural fractures (Clark et al., 2013). Low porosity and permeability in the Hartselle Sandstone are indicative of enhanced cementation (Clark et al., 2013). This is potentially due to a subtle anticlinal structure in the area resulting in enhanced precipitation of quartz cement at the crest of the structure (Wood, 1984). The core analysis of fluid saturation within the Hartselle Sandstone is as follow (Clark et al., 2013):

- Oil saturation within the Hartselle Sandstone core ranges from 2 to 61%. The average saturation is 24%, with a standard deviation of 13%.
- Water and oil saturation are negatively correlated with a regression coefficient of -0.71.
- Gas saturation ranges from 2 to 68%. The average saturation is 42%, with standard deviation of 15%.

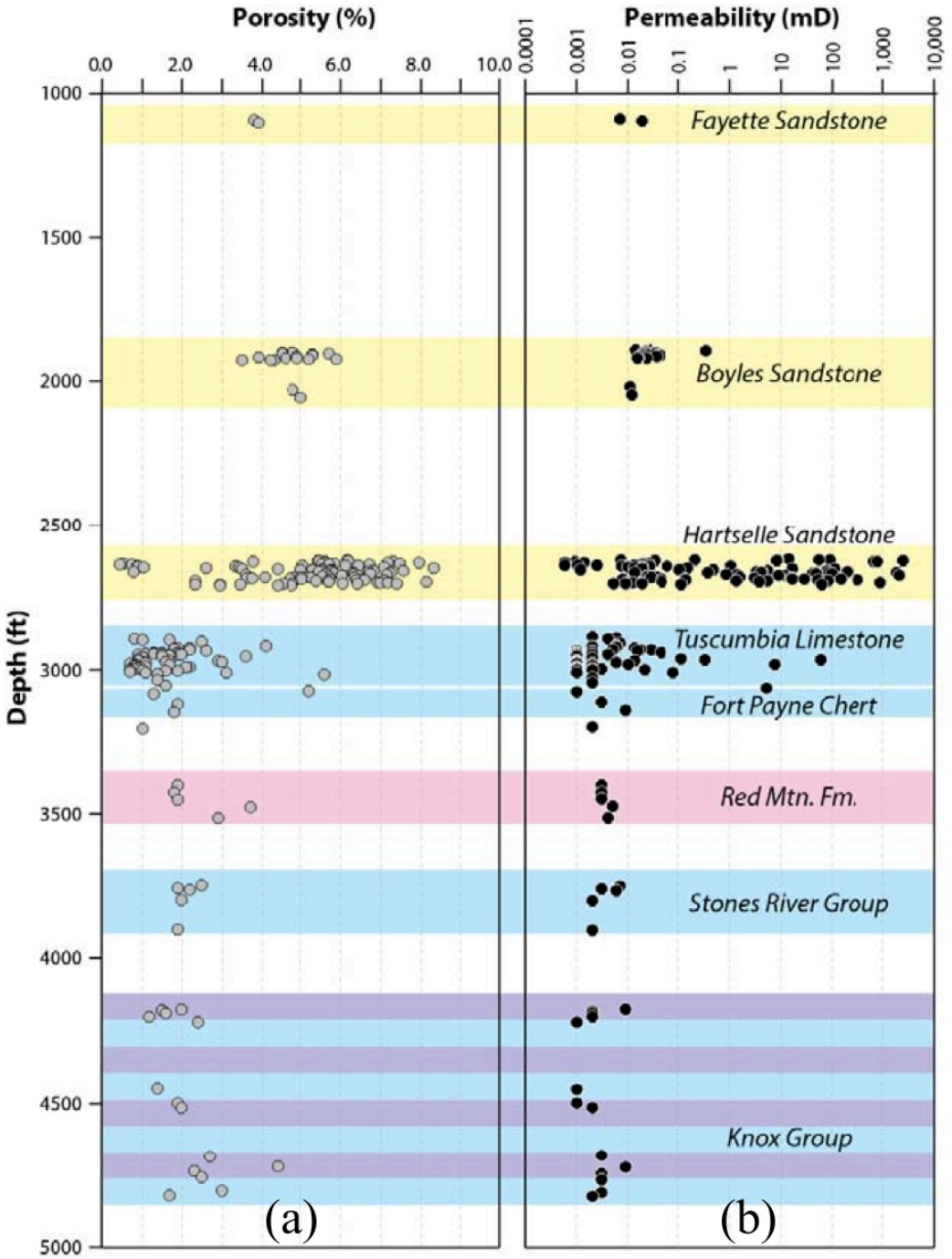

Figure 2.8. Plots of porosity (%) and permeability (mD) versus depth in the Gorgas #1 borehole from Clark et al. (2013), based on results from conventional core analysis. The Hartselle Sandstone contains a wide range of porosity and permeability.

CHAPTER 3: AVO

3.1 Hydrocarbon Detection using AVO

An important technique for detection of hydrocarbons is bright spot (amplitude anomaly) evaluation using AVO analysis (Ostrander, 1984; Estill and Wrolstad, 1993). Bright spots or high reflectivity zones in a seismic section are often associated with gas sands due to a high impedance contrast at a layer boundary (Dey-Sarkar and Svatek, 1993). However, bright spots can also be caused by, for example, other lithologic changes, such as coal seams or over-pressured shales (Dey-Sarkar and Svatek, 1993). AVO can be used to differentiate false bright spots from those associated with hydrocarbons based on the concept of differential behavior of P-wave velocity (V_p) and S-wave velocity (V_s) in hydrocarbon-saturated sands (Dey-Sarkar and Svatek, 1993). V_p and V_s responses in porous hydrocarbon-saturated rocks differ from those in other lithologies (Dey-Sarkar and Svatek, 1993). Moreover, the characteristically low ratio of V_p/V_s of hydrocarbon-saturated sands allow their differentiation from other low impedance layers such as coals or porous brine sands (Castagna, 1993). The interpretation of AVO for the detection of hydrocarbons has been verified in field tests by Ostrander (1984), Chiburis (1993), Estill and Wrolstad (1993), Avseth et al. (2016), and many others. Since the successful application of AVO by Ostrander (1984), AVO analysis has been widely used in hydrocarbon detection throughout the world with varying degrees of success (Chopra and Castagna, 2014).

3.2 AVO Intercept-Gradient Analysis Theory

3.2.1 AVO Attributes: Intercept and Gradient

As the name implies, AVO is the amplitude variation with offset, where the offset is the distance between the source and the receiver. P-wave amplitude at a reflector separating two media is known to vary with angle of incidence. Figure 3.1 shows the relationship between the offset and the angle of incidence as well as a simplified illustration of the partitioning of the energy of a P-wave as it reaches a reflector and returns to the receiver (Chiburis et al., 1993). AVO theory originates from the Zoeppritz (1914) equation, which describes how both P- and S-wave transmission and reflection coefficients vary with the incident angle of the ray path as they are reflected from a planar interface between homogenous media (Swan, 1993). In the Zoeppritz

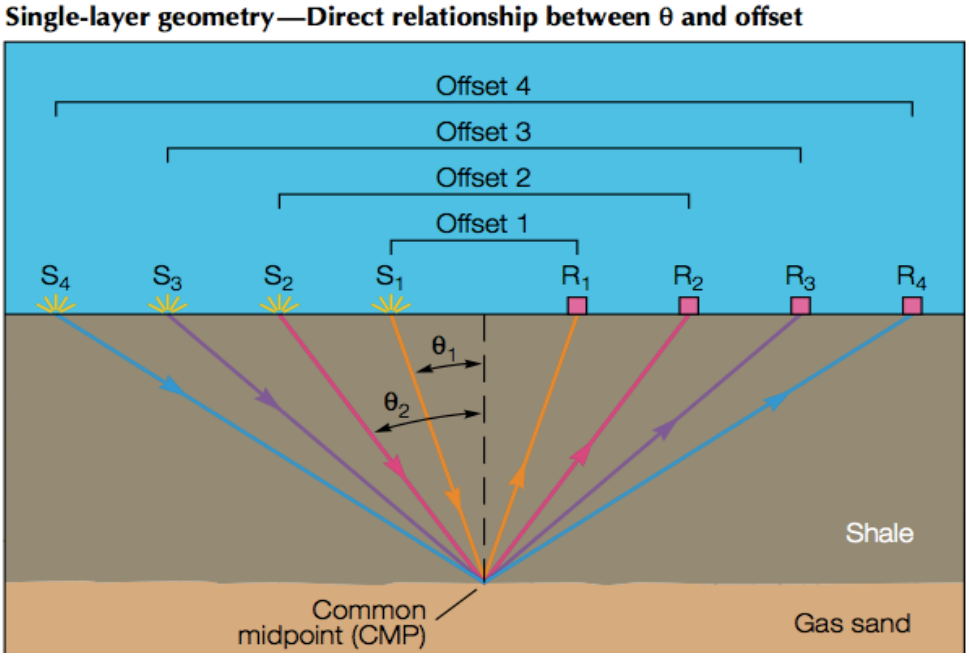

Figure 3.1. Single layer geometry showing the relationship between the angle of incidence (θ) and offset. From Chiburis et al. (1993).

equation, reflection coefficients are equivalent to amplitudes, in the absence of effects such as transmission losses, attenuation, divergence, and geophone directivity (Chopra and Castagna, 2014). Additionally, there are four independent variables at an interface: V_p, V_s, density, and

Poisson's ratio of the upper and lower media. Koefoed (1955) observed large changes in P-wave reflection coefficients versus offset by applying different Poisson's ratios to two bounding media in the Zoeppritz equations. The pronounced influence of Poisson's ratio on how the reflection coefficients varied with offset gives rise to the practical AVO analysis that is widely used today (Chopra and Castagna, 2014). AVO responses are directly related to contrasts in acoustic impedance and Poisson's ratio, which in turn correspond to changes in rock properties and in-situ fluid saturations (Estill and Wrolstad, 1993). Other AVO attributes include AVO intercept (i.e., the reflection coefficient at zero angle of incidence), AVO gradient (i.e., the change in the reflection coefficient with the square of the angle of incidence), Lamé parameter (λ), shear modulus (μ), and fluid factor (Swan, 1993). AVO attribute analysis examines AVO anomalies in a pre-stack seismic line. This process includes multiple methods, such as near and far stacks, intercept-gradient analysis, and the fluid factor. This study employed the intercept-gradient analysis method, which measures and plots the amplitude of the signal for a target horizon against the offset of the trace (or the corresponding angle that the seismic wave travels as it reflects from a reflector).

3.2.2 AVO Crossplots

In AVO analysis, the anomalous relationships between V_p, V_s, and density in hydrocarbon-bearing rocks differ from those relationships in brine-saturated rocks (Chopra and Castagna, 2014). Thus, anomalous AVO gradients are useful as a hydrocarbon indicator when compared against the gradient of equivalent brine-saturated rocks. Crossplots between AVO attributes are useful in identifying anomalous off-trend accumulations that could be related to hydrocarbons (Chopra and Castagna, 2014). A common AVO crossplot compares the intercept (*i.e.*, the reflection coefficient at zero angle of incidence) to the gradient (*i.e.*, the change in the

reflection coefficient with the square of the angle of incidence) (Figure 3.2; Foster and Keys, 1999). AVO slope and intercept are estimated by fitting AVO attributes to a curve relating to $\sin^2(\theta)$, where θ denotes the angle of incidence (Hong et al., 1993). The slope of the crossplot can be interpreted as a change in Poisson's ratio within the reservoir zone (Yilmaz, 2001). Hence, an increase in the slope suggests an increase in the change of the Poisson's ratio, which in turn, can be related to hydrocarbon-saturated reservoir sands (Yilmaz, 2001).

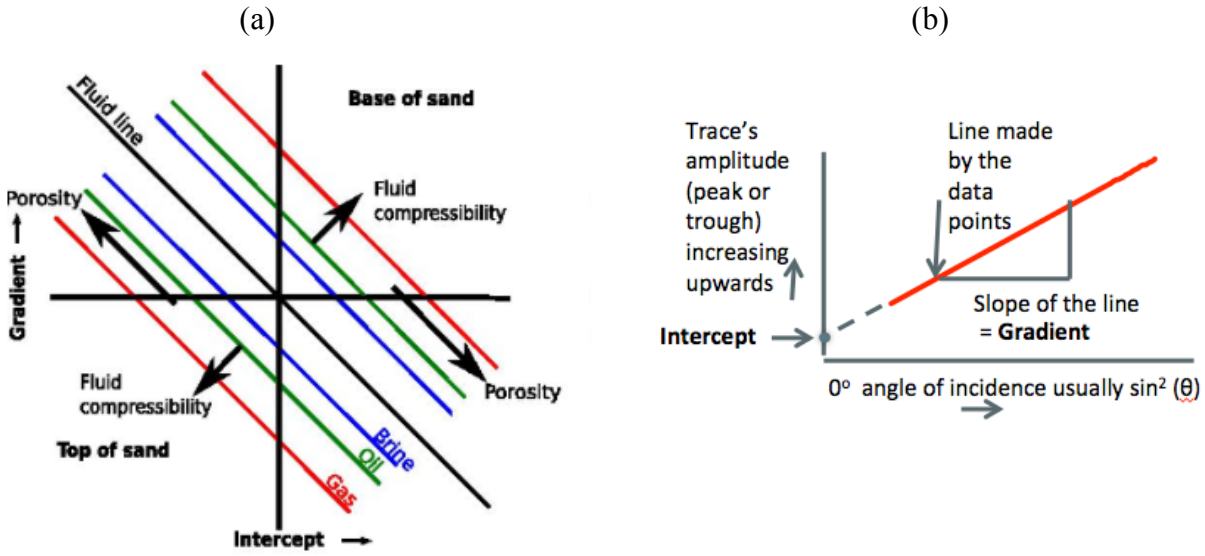

Figure 3.2. (a) AVO intercept vs. gradient crossplot adapted from Foster and Keys (1999). showing top and base of sand, which includes the porosity and fluid compressibility. (b) A gradient curve showing the definition of AVO intercept and gradient, where $\sin^2(\theta)$ is plotted in the x-axis and amplitude is plotted on the y-axis.

CHAPTER 4: DATA AND METHODS

There are three parts to the AVO technique performed in Geoview (a part of the Hampson-Russell package): seismic conditioning, forward AVO modeling (synthetic modeling), and seismic reflection data analysis or AVO analysis. For the seismic conditioning and the AVO analysis, two pre-stack 2-D seismic reflection lines collected near Gorgas Power Plant were used. For the synthetic modeling phase, a suite of well logs from Gorgas #1 were used. In addition, check-shot data were used for well-log correction. Well logs, seismic reflection data, and check-shots were imported into Geoview.

4.1 Data

4.1.1Seismic Reflection data

The 2-D Vibroseis land seismic reflection survey located in Jasper, Alabama, consisted of two 8.05 km (5 miles) lines (Figure 1.4). Line 101 runs north-south along Country Road 6. This road is winding and has large elevation variations, resulting in processing issues and challenges. Increased noise levels in the center of line 101 coincide with a topographic high, which is adjacent to vertical faces associated with coal mine high-walls adjacent to the road (Figure 4.1; Clark et al., 2013). Line 201 runs northeast-southwest along State Highway 269, which is the closest line to the Gorgas #1 well (1.28 km or 0.795 miles north of the well site) (Figure 4.2; Rutter, 2012).

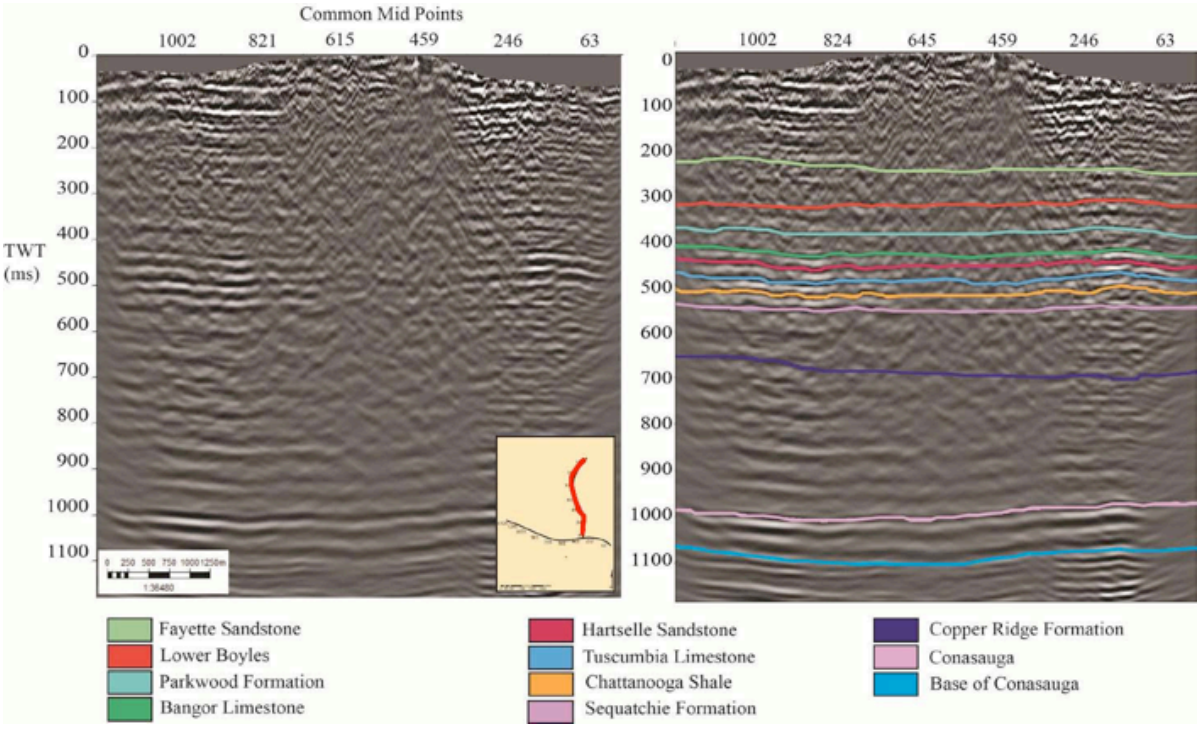

Figure 4.1. Post-stack time migrated 2-D seismic reflection profile for line 101 from Rutter (2012).The profile is oriented north to south. CMP spacing is 6 m (20 ft). The vertical scale is TWT in milliseconds (ms). The profile passes over a topographic high between CMPs 896 and 288.

Two anomalous zones along line 201 at common mid-point (CMP) 237 and CMP (781) coincide with bridges along the road, which required a gap in the receiver distribution (Rutter, 2012). The locally low-fold CMPs preclude good velocity picks and corrections to normal moveout (NMO), which cause the anomalous dips in these area (Rutter, 2012). The maximum offset between source and receiver was 8047 m (26,400 ft) and the seismic bin size is 6 m (20 ft). The 2-D pre-stack seismic volumes used in AVO analysis have been processed to common depth point (CDP) gather stage by WesternGeco. The processing workflow is included in Appendix I. Since the seismic reflection data were collected using a Vibroseis source, the seismic reflection data are zero-phase (Rutter, 2012).

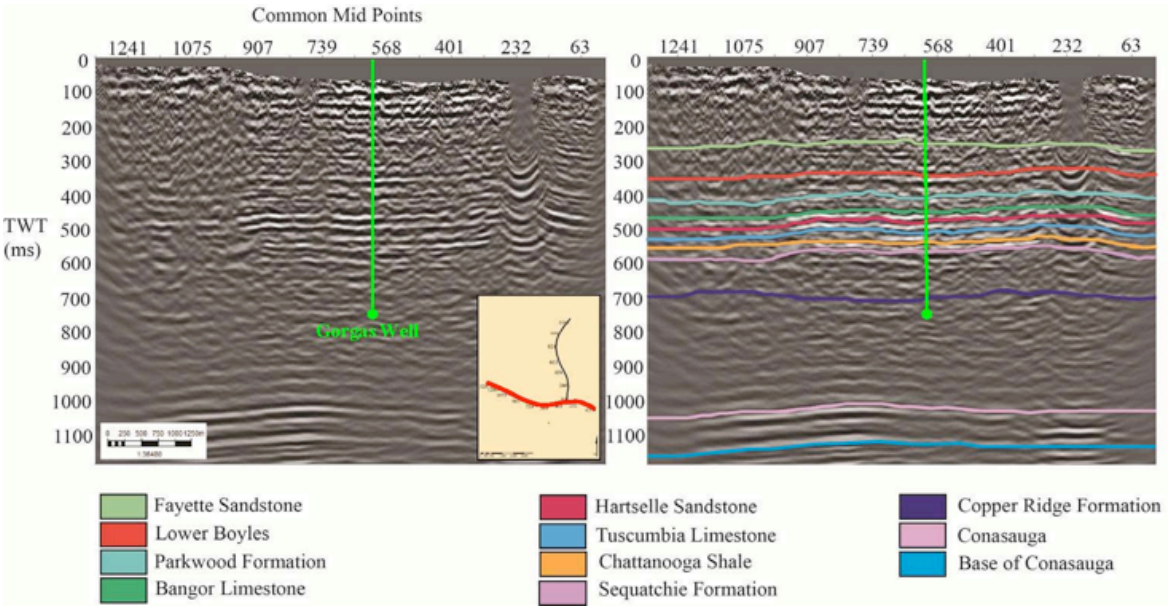

Figure 4.2. Post-stack time migrated 2-D seismic reflection profile for line 201 from Rutter (2012). The profile is oriented north to south. CMP spacing is 6 m (20 ft). The vertical scale is TWT in milliseconds (ms). The location nearest to the well is at CMP 576. The well reached a total depth of 4915 ft (700 ms) coincident with the Copper Ridge Formation. Reflector disturbance under CMP 232 is due to traces being removed because of a bridge on the receiver path.

As with any seismic reflection data, tuning occurs due to low vertical resolution of the seismic data, which presented a challenge in resolving the top and bottom reflection events. As an example, Table 1 illustrates the vertical resolution of the Hartselle Sandstone in the seismic reflection data, which is calculated from the known velocity of the Hartselle Sandstone and peak frequency. Since the Hartselle Sandstone from the Gorgas #1 borehole is 26.5 m (87 ft) thick, the vertical resolution of the seismic reflection data of 45 m (146 ft) only allows the interpreter to detect the Hartselle Sandstone reflection but not to fully resolve the top and bottom of the formation. For conducting the AVO analysis, the 2-D pre-stack time migrated offset gathers of both line 101 and 201 were used. These data needed further conditioning before performing AVO analysis.

Table 1
The Vertical Resolution Calculation of the Hartselle Sandstone Interval from the Seismic Reflection Data. Vertical Resolution Equals a Quarter of Wavelength.

Hartselle Sandstone velocity	5094.9 m/s (16715.5 ft/s)
Peak frequency	30 Hz
Wavelength	169.8 m (577.2 ft)
Vertical resolution	42.5 m (139.4 ft)

4.1.2 Well log data

Starting at a surface elevation of 114.65 m (376 ft), the Gorgas #1 well was drilled to a total depth of 1498 m (4915 ft) in the Upper Cambrian Copper Ridge Formation (Figure 2.2; Clark et al., 2013). A variety of geophysical well logs were collected by Schlumberger Carbon Services. V_p, V_s, and density logs (Appendix II) were used in this study for the well-seismic tie and for creating synthetic seismograms during the synthetic modeling phase.

4.1.3 Check-shot

Check-shot data provide a time-to-depth conversion and are useful for AVO analysis to identify the target depth for analysis and modeling. The check-shot survey was conducted using the Vibroseis source located 49 m (162ft) horizontally to the northwest of the well and 4.18 m (13.74 ft) below the Kelly Busing (KB; Rutter, 2012; Figure 4.3). The downhole measurements were recorded at an interval of 15 m (50ft) between 30 and 478 m (100-4850 ft) depth (Rutter, 2012). The check-shot report (Appendix III) provides vertical one-way transit time corrected for source offset with the static correction applied, depths from KB and from seismic reference datum (SRD; 244 m (800 ft) above sea level), acoustic velocity average to that depth, root-mean-square (RMS) velocity, and interval velocities calculated for each measurement interval (Rutter, 2012). In this study, the vertical one-way transit time corrected for source offset and the depths

from KB from the check-shot report were used to calibrate with the V_p log.

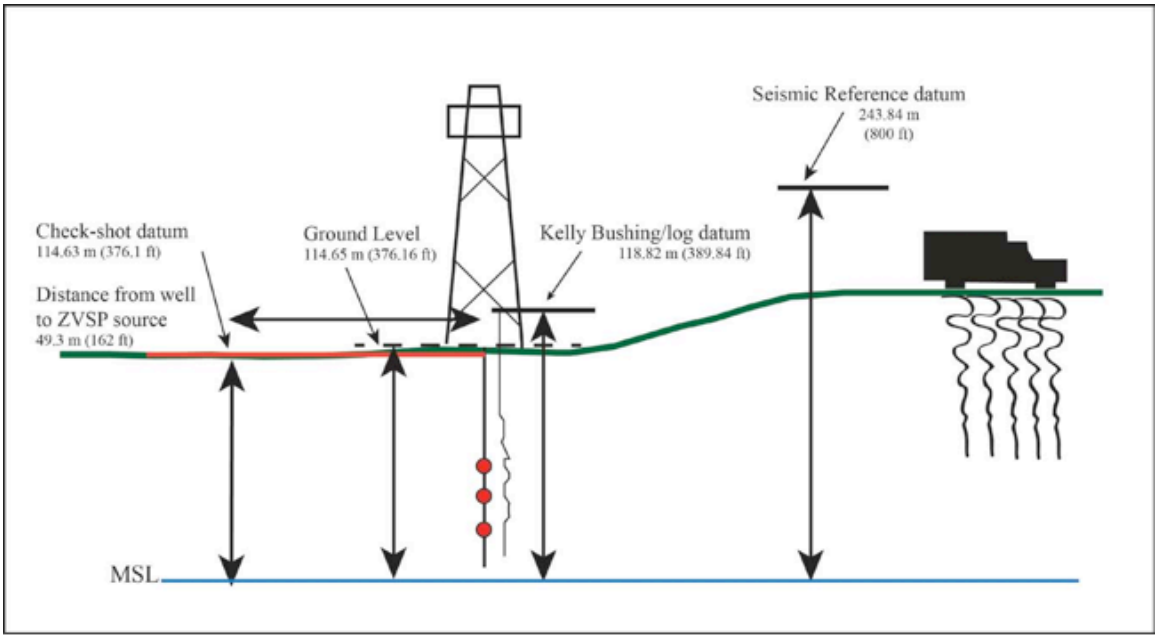

Figure 4.3. Diagram from Rutter (2012), showing different datum elevations for seismic reflection data (SRD) check- shot data, well log data (KB), and ground level relative to maximum sea level (MSL). The source location for the check-shot relative to the well is also shown.

4.2 Seismic Conditioning for AVO

Pre-stack conditioning of seismic reflection data for AVO analysis is important - as there are many possible ways to distort seismic amplitudes and mask AVO information during seismic processing. To derive the best AVO results, the pre-stack data should be appropriately pre-conditioned. Even though the two 2-D pre-stack seismic sections have already been preprocessed, data conditioning is necessary to further remove noise from the seismic reflection data and to flatten reflection events for a more accurate AVO attribute extraction. The following data conditioning workflow, a part of the conditioning process in Hampson-Russell, is designed to reduce noise in the seismic reflection data and is valid for this particular data-set.

4.2.1 Data conditioning workflow: supergather, trim statics, muting

The data conditioning workflow described in this section was applied to both seismic reflection line 101 and 201 to prepare the data for AVO analysis. Supergather formation is the process of combining a given number of adjacent CDP gathers to enhance the signal-to-noise ratio and ensure that all offsets are populated (Chopras and Castagna, 2014). In this process, a number of supergathers were calculated in which each trace represents a range of offsets. There are 73 offsets centered between CDP 180-8820 at CDP 239,349,476…8642,8761. To perform an AVO analysis, reflections events should be flattened, which can be corrected by the NMO correction. However, there are limitations in the NMO correction process due to issues with velocity analysis. Additionally, the NMO correction also leaves residual move-out errors (RNMO) that distort the estimation of AVO attributes. To correct these errors and to flatten the reflection events, a trim statics process was performed on the already NMO-corrected seismic gathers from lines 101 and 201. Trim statics is a process that applies an optimal time shift. This time shift is determined by cross-correlating each trace with a reference trace (Hampson, 2004). In this process, a pilot trace, which is usually the stacked trace, was created using the Trim Statics correction tool in Geoview. This pilot trace was then used to correlate with each trace in the pre-stack gather using a group of sliding windows (Fadolalkarem, 2015). The optimal time shift for each window was determined by the cross-correlations in that window and the time shift was then applied to each trace to create horizontally aligned events. Afterwards, a mute was applied to a range of pre-stack gathers to eliminate noise in the far offset. This is done by manually picking the traces to be muted. The mute traces selected were then removed from the gathers, which ensured that only the reliable data for AVO analysis remain.

4.3 Well-Seismic Tie

To obtain time-to-depth relationships and to determine the location of the Hartselle Sandstone horizon within the seismic reflection data for AVO analysis and AVO forward modeling, a well-seismic tie was performed. A well-seismic tie is a method of relating the well log data (measured in depth) to seismic data (measured in two-way travel time). This method offers a direct tie between the seismic data and the geologic data (Figure 4.4; Stommel and Graul, 1978). A zero-offset synthetic seismogram, a simulated seismic section created from the well data, was correlated with the seismic reflection data.

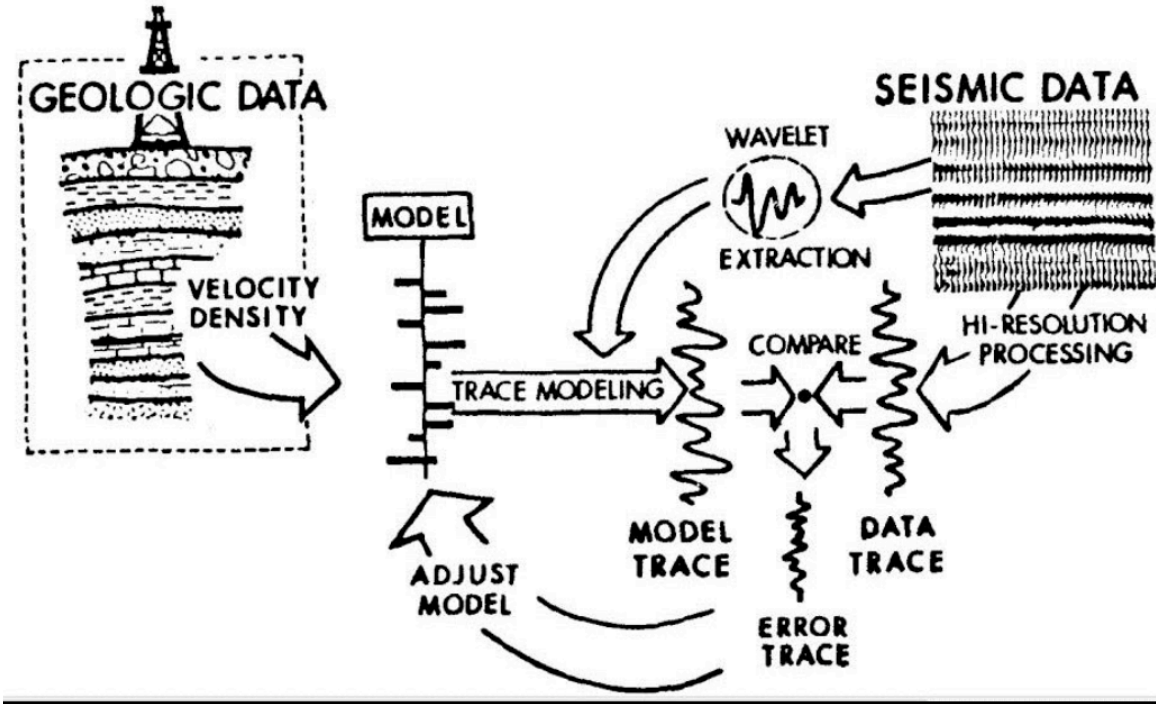

Figure 4.4. Flow chart for the well-seismic tie from Stommel and Graul (1978). The synthetic seismogram was created by convolving a reflectivity series computed from well logs, with a wavelet extracted from the seismic reflection data. The synthetic were then matched with the data trace. V_p and density logs were used in this part of the study.

Since seismic reflection line 201 is closest to the well location, it was selected for the well-seismic tie. To create the zero-offset synthetic seismogram, the reflectivity series was calculated using the check-shot calibrated sonic and density logs, which were convolved with the

extracted zero-phase wavelet from the 2-D seismic reflection data. The log-correlate function in Geoview allows for matching of the key reflectors between the synthetic trace and the seismic reflection data. The location of formation tops in the log measurements were input into Geoview. Since the formation top of the Hartselle Sandstone is known from the log, the key reflector representing the Hartselle Sandstone could be identified in the seismic reflection data.

4.4 AVO Intercept-Gradient Analysis

The AVO intercept-gradient analysis workflow was performed in. First, the final migrated CDP gathers from seismic line 201 were selected. The Hartselle Sandstone horizon was picked at the peak (positive amplitude) at 490 ms (TWT) in the seismic section and was selected for analysis. A velocity model was created using the edited V_p log. The seismic reflection data were then transformed from offset gathers to angle gathers by applying the velocity model. Finally, AVO intercept-gradient analysis was applied to the Hartselle Sandstone horizon. intercept and gradient attributes were extracted from this step. AVO crossplots were generated, which plot the intercept (i.e., amplitude at zero angles of incidence) on the x-axis and the gradients on the y-axis. The zone of hydrocarbons was interpreted and outlined in the AVO crossplot. An AVO attribute volume was then generated. This workflow was applied to both lines 101 and 201.

4.5 AVO Forward Modeling

The AVO forward modeling workflow was also performed in Geoview. Edited sonic logs, the density log, and the line 201 seismic reflection data were used for modeling. A statistical wavelet, extracted previously from the well-seismic tie, was also selected. A reflection coefficient series was generated from the V_p, V_s, and density logs. These were then convolved with the extracted seismic wavelet to generate synthetic models. Unlike the synthetic created

previously for the well-seismic tie, AVO forward modeling aims to create offset or angle gather synthetic seismograms resulting from the borehole's petrophysical and fluid parameters. To do this, the percentage of fluid content within the reservoir to model was specified (24% oil, 42% gas, and 34% water from the Clark et al. (2013) core log analysis). The depth of the reservoir interval was specified (2599.83 ft to 2688.76 ft measured in depth from the surface). The time interval for the synthetic was specified (from 0 to 800 ms TWT). Finally, the rock matrix properties were specified (sandstone). The wavelet was convolved with the selected logs to create synthetic traces. The Zoeppritz equation was applied in order to model the AVO responses along the Hartselle Sandstone and create the pre-stack synthetic in the angle gather domain. AVO analysis was performed along the Hartselle Sandstone horizon within this pre-stack synthetic by following the AVO intercept-gradient analysis workflow (see section 4.4). Fluid substitution was also performed as a quality control tool (Mavko et al., 1995). Fluid substitution is based on the Biot-Gassman equations (Gregory, 1977), which simulate the AVO effects of different petrophysical and fluid values by creating synthetic seismograms. Using V_p, V_s, density logs, and the Biot-Gassman equations in Geoview, three additional pre-stack synthetic seismograms were generated to simulate the AVO effects of pure brine (100% brine saturation), pure oil (100% oil saturation), and pure gas (100% gas saturation) in the Hartselle Sandstone reservoir. AVO analysis was also performed along the Hartselle Sandstone horizon within these pre-stack synthetic seismograms.

4.6 Volumetric Analysis

The volume of hydrocarbons stored within the Hartselle Sandstone in the vicinity of the Gorgas Power Plant was estimated by first evaluating the extent of the potential hydrocarbon zones within the Hartselle Sandstone horizon outlined in the two seismic reflection profiles.

Since the CMP spacing is known (6m (20ft)) and the extent of the potential hydrocarbon zones were observed across the seismic lines, the total lateral extent of this hydrocarbon layer was determined. The radius of this extent is calculated by dividing this lateral extent in half. The bulk volume of the Hartselle Sandstone reservoir in this area was estimated by approximating the area as a disk (area=π*radius^2) and the thickness of the reservoir as 26 m (86 ft), which is consistent with the thickness of the Hartselle Sandstone layer within the Gorgas #1 core. For the volumetric and risk assessment, which was performed separately for each seismic reflection section, the Rose and Associates risk analysis package was used. This package is a series of Excel macros which allow the potential hydrocarbon volume and chance of success to be estimated from input components related to reservoir properties, based on Rose & Associates' volumetric and chance estimating methods (Rose, 2001). Free hydrocarbons were determined by entering the range of values in the Rose and Associates multi-method risk analysis package. These values include the areal extent estimated from the seismic reflection data, the core thickness, the porosity, and the hydrocarbon saturation, as determined by the Clark et al. (2013) core analysis of the Hartselle Sandstone.

CHAPTER 5: RESULTS

5.1 Seismic Conditioning Results

The CDP from line 101 before seismic conditioning (Figure 5.1a) shows that individual reflectors have large variations in amplitude with offset. Some reflectors show poorly defined and poorly aligned seismic reflection events. For example, at approximately 490 ms, a reflector with positive amplitudes lacks continuity around the near offset traces from 180 ft to 2820 ft. Some trace amplitudes between 1380 and 2820 ft are slightly misaligned compared with the rest of the trace amplitudes beyond 2820 ft. The reflectors below 500 ms curve downward, indicating the effect of NMO that has not been fully corrected during the velocity analysis in the processing workflow (Appendix I). On the other hand, the CDP after seismic conditioning (Figure 5.1b) shows that individual seismic reflectors are better aligned, particularly around the reflector at 490 ms, where the reflector is continuous and aligned horizontally. Far trace amplitudes are noisy and will contaminate the AVO attribute calculation; therefore, these were removed by muting these traces. For example, the traces between about 3000 and 7000 ft offset and between 300 and 500 ms were muted. The reflectors below 500 ms still curve downward due to NMO effects. Nevertheless, seismic conditioning along line 101 has improved the data for AVO analysis, especially the reflectors above 500 ms around the target area of this study.

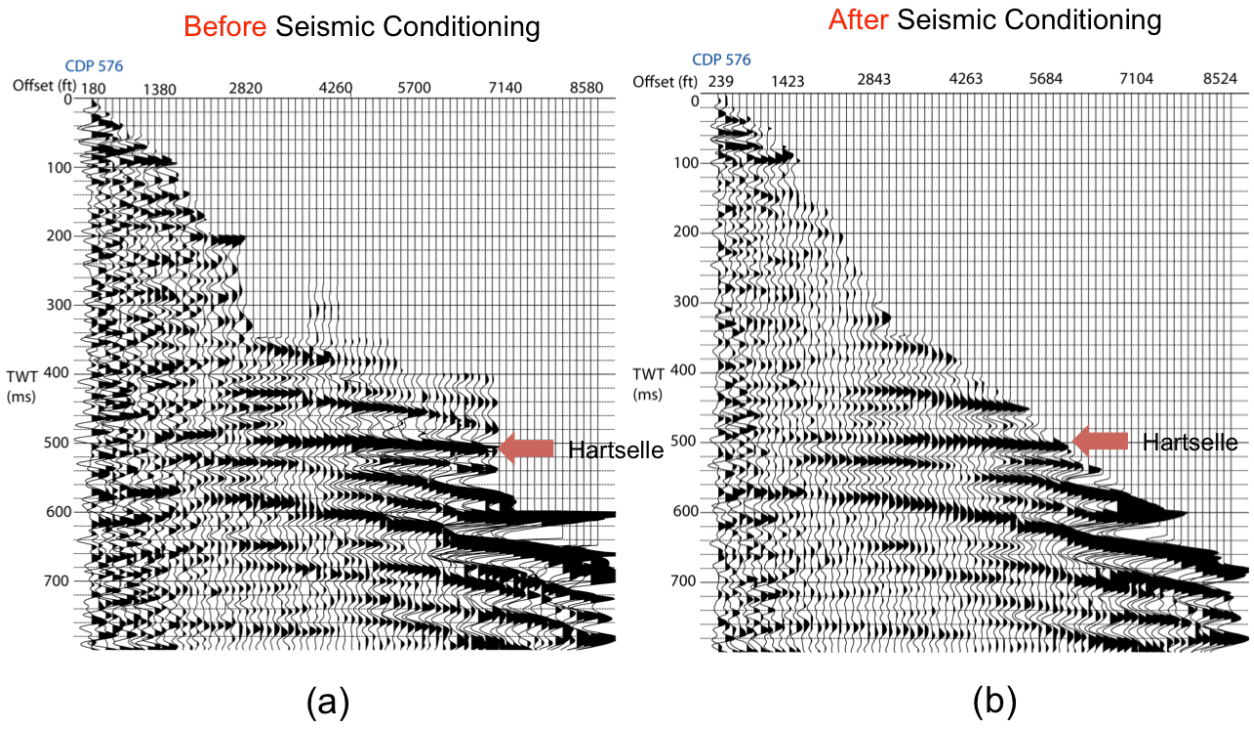

Figure 5.1. CDP 576 of the pre-stack seismic reflection profile for line 101. (a) shows the CDP before seismic conditioning and (b) shows the CDP after seismic conditioning. The reflector corresponding to the Hartselle Sandstone is marked with a red arrow.

Similar to Figure 5.1, Figure 5.2 illustrates a CMP from line 201 before and after the application of seismic conditioning. The data quality of line 201 is better than line 101 in terms of trace amplitude alignment and reflector definition. Before seismic conditioning (Figure 5.2a), the peak reflector at approximately 490 ms contains high amplitude traces that are aligned but with a gentle dip from about 2100 to 5000 ft. Additional reflectors below 500 ms curve downward less than those of line 101, indicating the NMO effect is not as great. After seismic conditioning (Figure 5.2b) the data show significant improvement in terms of trace alignment and reflector definition. Seismic conditioning removed the background noise, making individual reflectors clearer. The gentle dip along the peak reflector at approximately 490 ms was flattened, and thus the reflector is continuous with increasing offset. Since the residual NMO effect is not as high on line 201 compared to line 101, the NMO was corrected and most of the reflectors

below 500 ms are flattened horizontally. Offset gathers along both lines 101 and 201 after seismic conditioning are ready to be converted to angle gathers for AVO analysis.

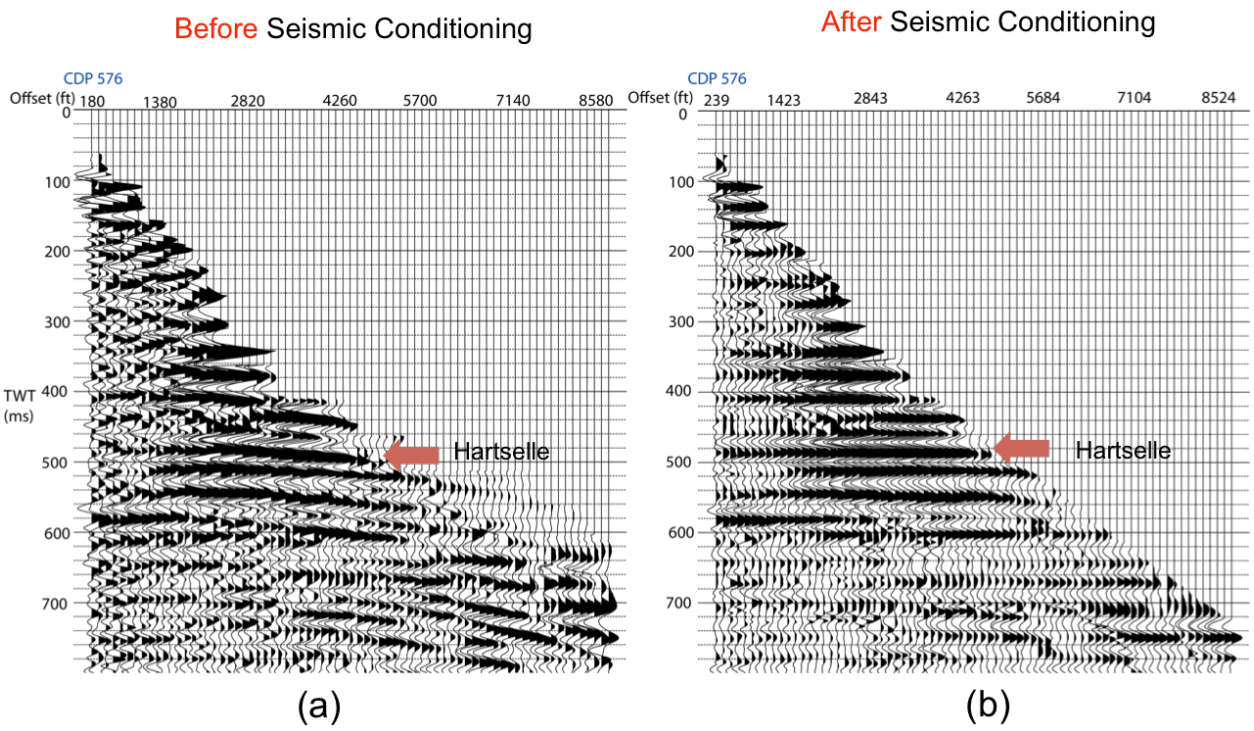

Figure 5.2. CDP 576 of the pre-stack seismic reflection profile for line 201. (a) shows the CDP before seismic conditioning and (b) shows the CDP after seismic conditioning. The reflector corresponding to the Hartselle Sandstone is marked with a red arrow.

5.2 Well-Seismic Tie Result

A zero-offset synthetic seismogram was computed in Geoview using V_p and density logs. This synthetic was matched with the seismic reflection data from line 201. Reflectors in the seismic reflection data correspond to changes in acoustic impedance due to lithologic transitions between and within limestones, shales, and sandstone. Synthetic reflectors, including both peaks (positive amplitudes) and troughs (negative amplitudes), were picked to match the peaks and troughs in the composite trace of the seismic reflection data during the well-seismic tie. The key tie points for the correlation include the high amplitude peaks that correspond to the Jefferson Coal, Fayette Sandstone, Upper Boyles, Lower Boyles, Hartselle Sandstone, Tuscumbia

Sandstone, and Chattanooga Shale (Figure 5.3). After the well-seismic tie, a time-depth relationship between the well data and the seismic reflection data was determined. The top of Hartselle Sandstone, identified at a measured depth (MD) of 2615 ft from KB in the well, is found to be at 476.4 ms in the seismic reflection data (Figure 5.3; Table 2). The entire Hartselle Sandstone unit is associated with the peak at 490 ms. Based on this, the interpretation of the Hartselle Sandstone was extended along each seismic line. The interpreted Hartselle Sandstone horizons from the seismic lines were then selected for the AVO intercept-gradient analysis.

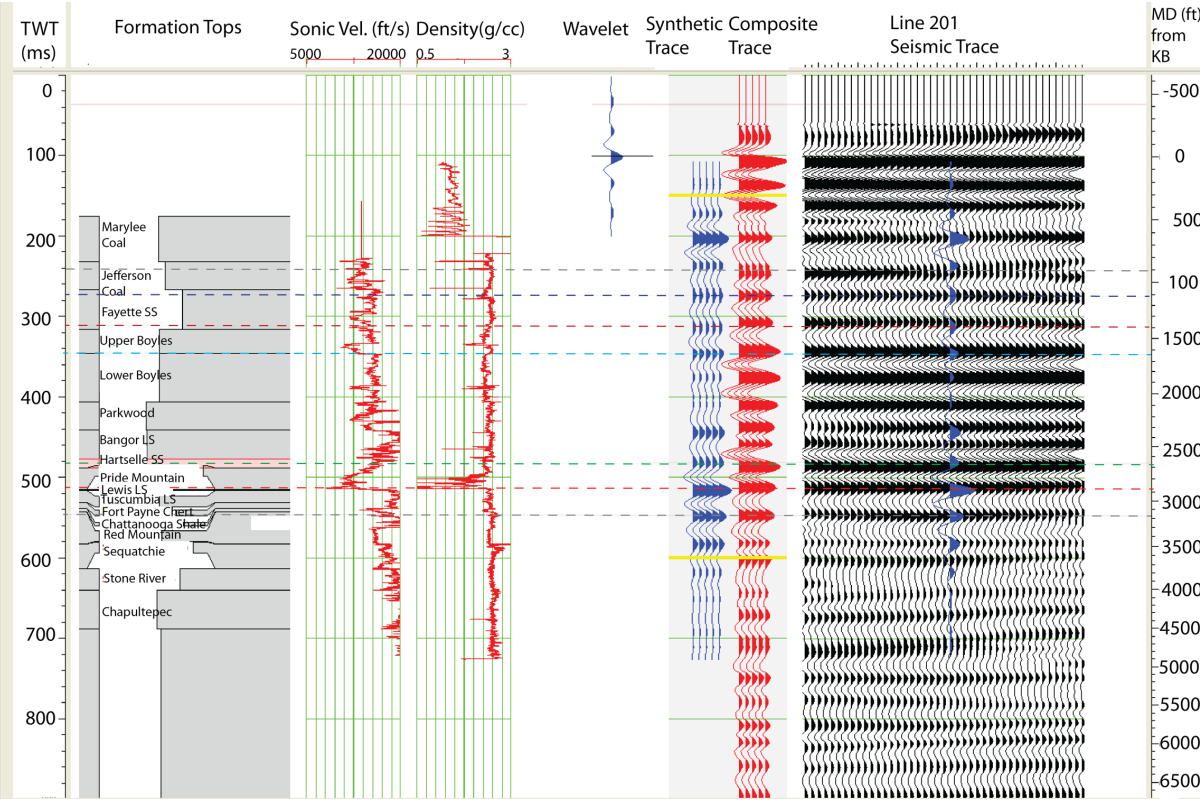

Figure 5.3. Zero-offset synthetic seismogram created in Geoview showing the formation tops, density, V_p logs, wavelet, synthetic traces (blue curves), composite seismic traces (red curves), and real seismic reflection data. The dashed lines indicate the key tie points. A time-depth relationship was obtained. TWT (ms) is displayed on the vertical axis on the left and MD (ft) from KB is indicated on the vertical axis on the right. The Hartselle Sandstone interval is highlighted in red within the formation tops column.

Table 2

*Measured Depth (MD) from Kelly Bushing (KB), True Vertical Depth (TVD) from Seismic Reference Datum (SRD), Average Velocity from SRD, RMS Velocity from SRD, and Interval Velocity of the Formation Tops at Gorgas Power Plant. ** Only Seen on Seismic.*

Top Name	MD from KB (ft)	Elevation (ft)	TVD from surface (ft)	TVD from SRD (ft)	Time from SRD (ms (Two Way time))	Interval	Time Interval (ms)	Average Velocity from SRD (ft/s)	RMS Velocity from SRD (ft/s)	Interval Velocity (ft/s)
Marylee Coal	469	-79.16	455.32	879.16	175.177	First curve entry to Marylee Coal	---	10037.4	10037.4	12744.6
Jefferson Coal	828	-438.16	814.32	1238.16	231.865	Marylee Coal to Jefferson Coal	56.6874	10680	10739.6	12665.9
Fayette Sandstone	1058	-668.16	1044.32	1468.16	266.519	Jefferson Coal to Fayette Sandstone	34.6546	11017.3	11101.9	13273.9
Upper Boyles	1416	-1026.16	1402.32	1826.16	315.781	Fayette Sandstone to Upper Boyles	49.2615	11566	11703.9	14534.7
Lower Boyles	1627	-1237.16	1613.32	2037.16	346.004	Upper Boyles to Lower Boyles	30.2232	11775.4	11918.3	13962.8
Parkwood	2071	-1681.16	2057.32	2481.16	406.153	Lower Boyles to Parkwood	60.1494	12217.8	12380.9	14763.2
Bangor LS	2320	-1930.16	2306.32	2730.16	441.126	Parkwood to Bangor LS	34.9727	12378.1	12538.3	14239.7
Hartselle	2615	-2225.16	2601.32	3025.16	476.423	Bangor LS to Hartselle	35.2967	12699.5	12894.3	16715.5
Pride Moutain Formation	2702	-2312.16	2688.32	3112.16	487.854	Hartselle to Pride Moutain Formation	11.4313	12758.6	12953.6	15221.4
Lewis Sandstone	2874	-2484.16	2860.32	3284.16	514.567	Pride Moutain Formation to Lewis Sandstone	26.713	12764.8	12949.7	12877.6
Tuscumbia LS	2888	-2498.16	2874.32	3298.16	516.231	Lewis Sandstone to Tuscumbia LS	1.66437	12777.8	12964	16823.2
Fort Payne Chert	3021	-2631.16	3007.32	3431.16	531.35	Tuscumbia LS to Fort Payne Chert	15.119	12914.9	13118.4	17593.7
Chattanooga Shale	3088	-2698.16	3074.32	3498.16	538.489	Fort Payne Chert to Chattanooga Shale	7.13818	12992.5	13209.1	18772.3
Red Mountain	3124	-2734.16	3110.32	3534.16	542.554	Chattanooga Shale to Red Mountain	4.06531	13027.9	13248.6	17710.8
Sequatchie Formation	3467	-3077.16	3453.32	3877.16	582.092	Red Mountain to Sequatchie Formation	39.5379	13321.5	13566.5	17350.4
Stone River Group	3746	-3356.16	3732.32	4156.16	613.199	Sequatchie Formation to Stone River Group	31.1077	13555.7	13821.6	17937.7
Chapultepec	4007	-3617.16	3993.32	4417.16	640.074	Stone River Group to Chapultepec	26.8745	13802	14101.6	19423.6
Copper Ridge	4500	-4110.16	4486.32	4910.16	687.792	Chapultepec to Copper Ridge	47.7179	14278	14652	20663.1
Conasauga	9250	-8860.16	9236.32	9660.16	N/A	Copper Ridge to Conasauga	N/A	1.#INF	1.#INF	See remarks **

5.3 AVO Attribute-Gradient Analysis Results

5.3.1 Offset Gathers to Angle Gathers Results

CDPs were transformed from offset domain to angle domain. The number of angle gathers is the same as the number of CDPs for each seismic line. Figures 5.4 and 5.5 show a CDP and the corresponding angle gather for lines 101 and 201, respectively. In both examples, the angles range from 2° to 44°. Unlike an offset gather, angle gathers contains less trace amplitudes along the reflectors. In the angle gather for line 101 between 100 and 400 ms, the individual reflectors are poorly defined (Figure 5.4). From 400 and 700 ms, individual reflectors become more apparent. A strong, nearly horizontally-aligned positive amplitude reflector at approximately 490 ms is interpreted to correspond to the Hartselle Sandstone. Similar to line

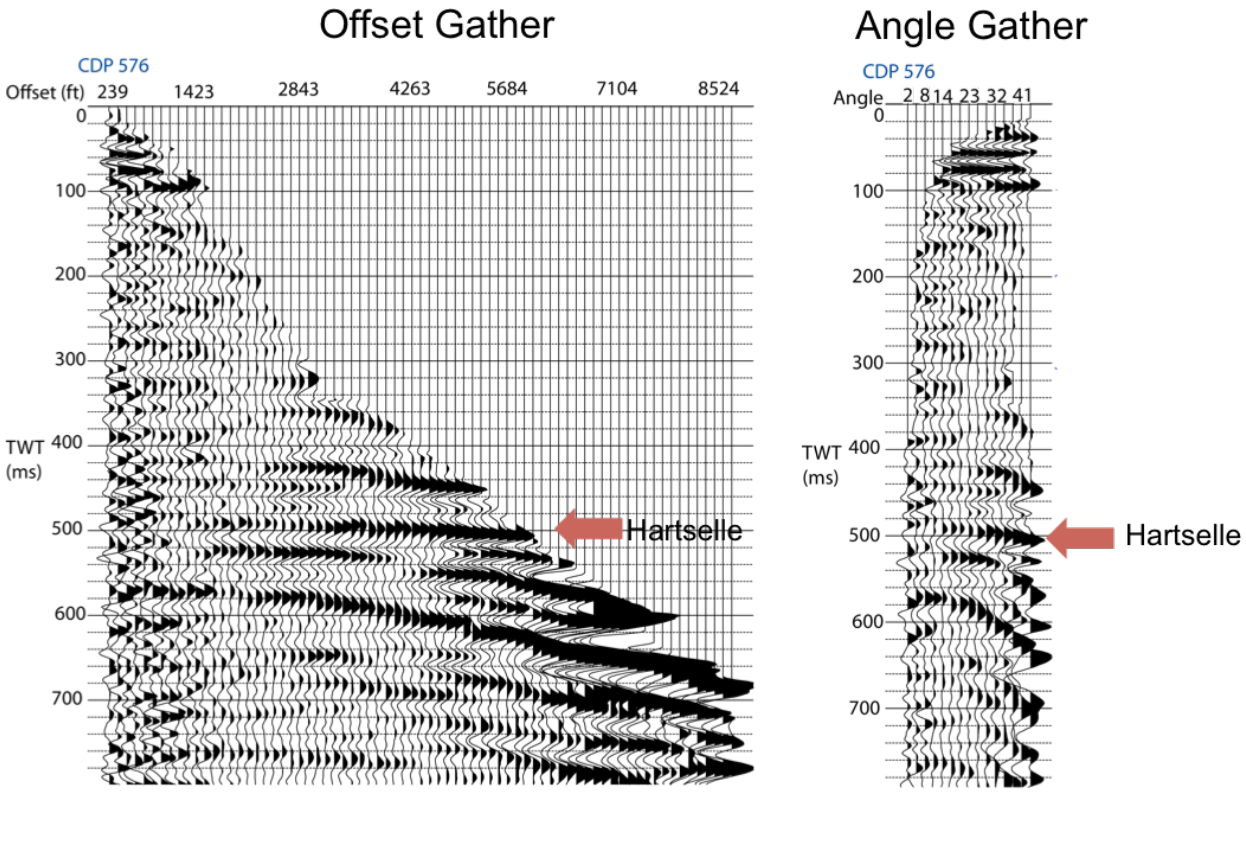

Figure 5.4. a) Offset gather at CDP 576 from line 101. (b) Angle gather at CDP 576 from line 101.

101, the line 201 angle gather also displays a horizontally-aligned positive amplitude reflector at approximately 490 ms, which is again coincident with the location of the Hartselle Sandstone horizon (Figure 5.5). Thus, the angle gathers for lines 101 and 201 are ready for the next step, which is AVO attribute analysis along the Hartselle Sandstone horizon.

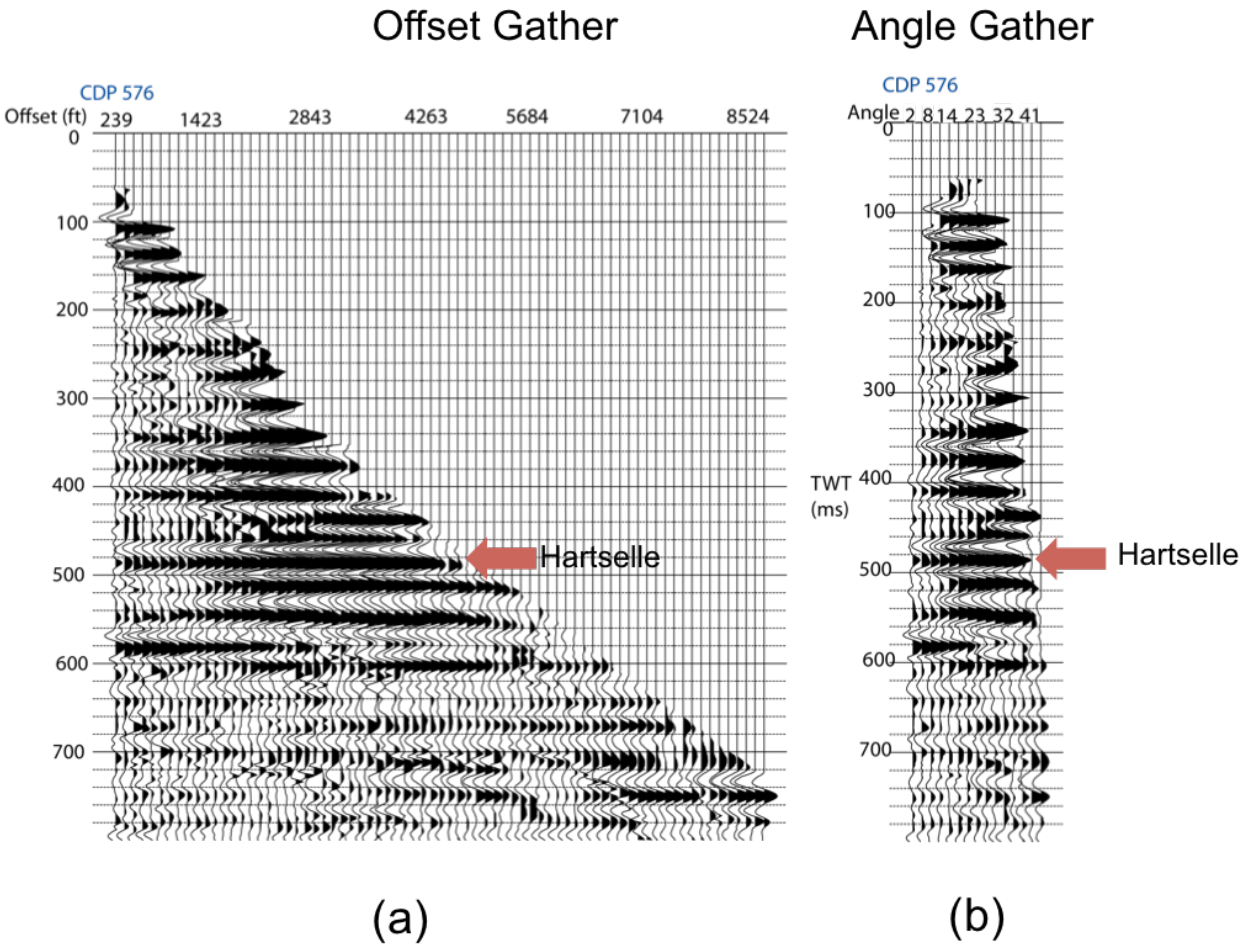

Figure 5.5. a) Offset gather at CDP 576 from line 201. (b) Angle gather at CDP 576 from line 201.

5.3.2 AVO Attributes Results (Intercept and Gradient)

AVO intercept-gradient analysis was performed along the Hartselle Sandstone horizon across CDPs from both seismic lines. Line 101 extends from CDP 6 to CDP 1173 and line 201 extends from CDP 6 to CDP 1328. The variation of amplitude with angle was evaluated to determine the intercept and gradient. From each angle gather for the Hartselle Sandstone horizon

across lines 101 and 201, these attributes were then plotted as shown on the crossplots (Figures 5.6 and 5.7).

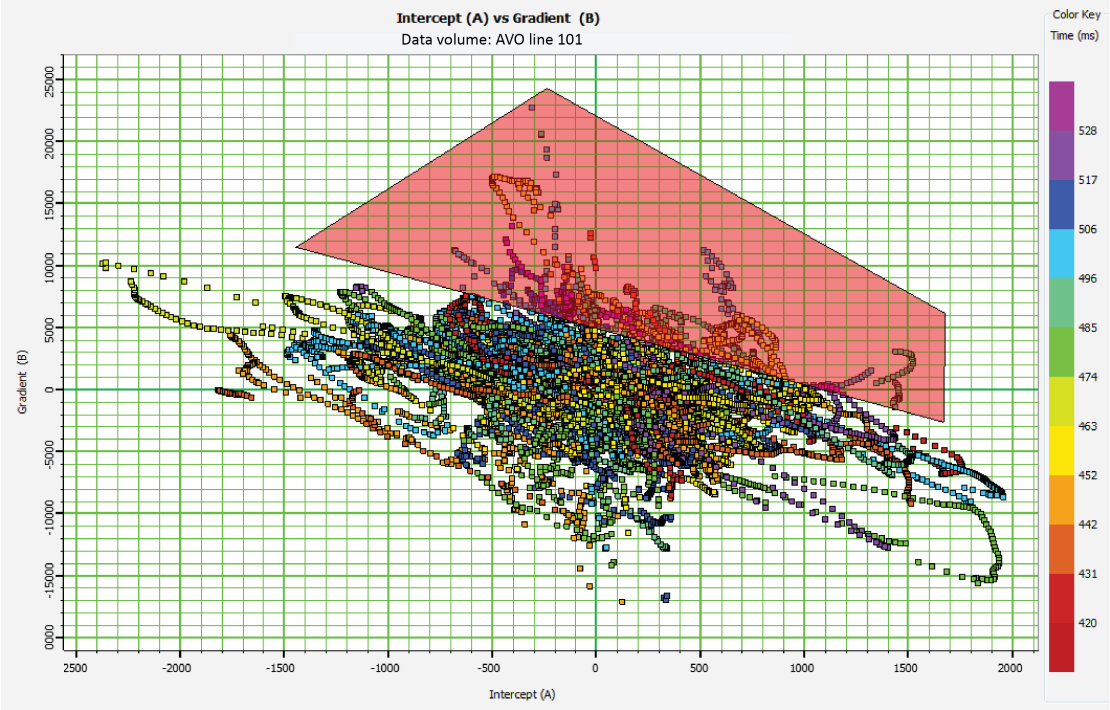

Figure 5.6. AVO intercept vs. gradient crossplot for the Hartselle Sandstone along line 101. The intercept (A) corresponds to the x-axis and the gradient (B) corresponds to the y-axis. The red polygon outlined as the zone of AVO anomalies, which is interpreted as a zone of potential hydrocarbons within the Hartselle Sandstone. The color key indicates the time (TWT) of the Hartselle Sandstone along the seismic line.

On line the 101 intercept-gradient crossplot (Figure 5.6), the data points cluster together near the center of the plot and have a negative trend that corresponds to the background trend. A similar trend is observed on the line 201 intercept-gradient crossplot (Figure 5.7). The AVO anomalies are data points that deviate from the background trend. The AVO anomalies above the background trend are outlined by red polygons in Figure 5.6 and 5.7. In lines 101 and 201, most of these anomalies concentrate in the first and second quadrant of the crossplots. The AVO

anomalies below the background trend are below the depth of the Hartselle Sandstone and therefore not relevant to this study.

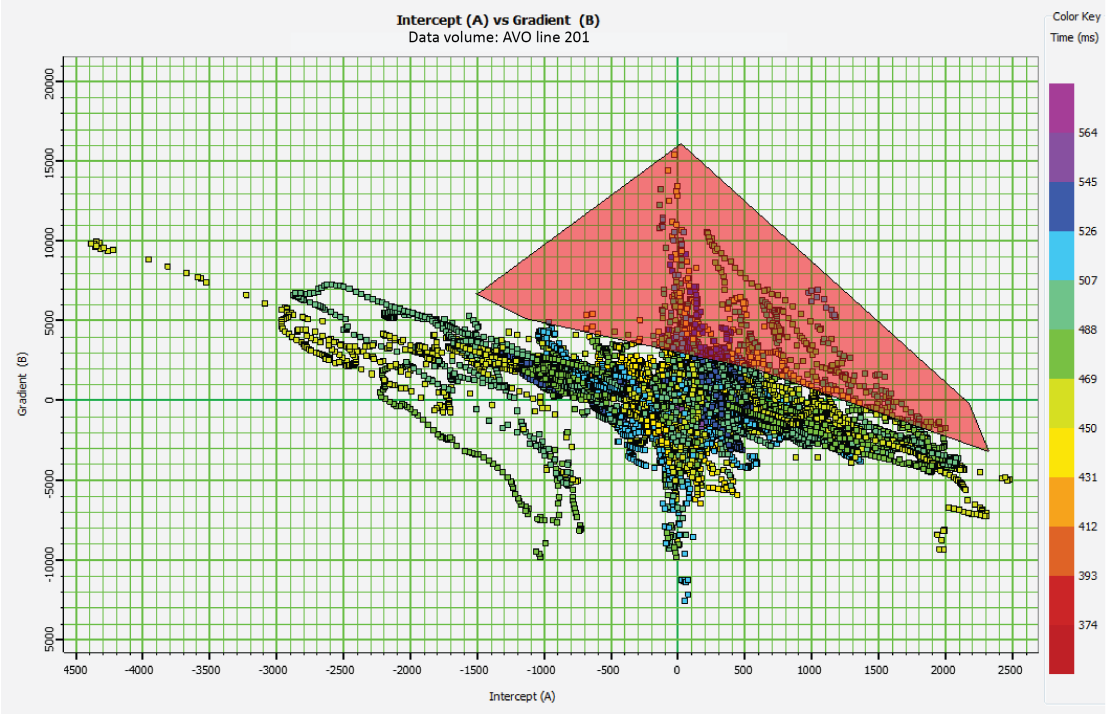

Figure 5.7. AVO intercept versus gradient crossplot for the Hartselle Sandstone along the line 201. The intercept (A) corresponds to the x-axis and the gradient (B) corresponds to the y-axis. The red polygon outlines zone of AVO anomalies, which is interpreted as a zone of potential hydrocarbons within the Hartselle Sandstone. The color key indicates the time (TWT) of the Hartselle Sandstone along the seismic line.

As mentioned in section 3.0, the background trend in the center of the crossplot is interpreted to correspond to brine-saturated sands. The AVO anomalies, which deviate from the background trend, are interpreted to correspond to hydrocarbon-saturated sands. The AVO attribute volumes for lines 101 and 201 were created (Figure 5.8 and 5.9). In each figure, the red polygon interpreted from the corresponding crossplot (Figure 5.6 and 5.7), or the potential hydrocarbon zone, was mapped throughout the seismic section. Although potential hydrocarbon zones are present throughout the attribute volume, this study only focuses on the Hartselle

Sandstone. In the line 101 attribute volume, the red layer along the Hartselle Sandstone horizon extends from CDP 16 to CDP 37, and from CDP 232 to CDP 310 (Figure 5.8). In the line 201 attribute volume, the hydrocarbon layer within the Hartselle Sandstone horizon extends from CDP 548 to CDP 646 and from CDP 732 to CDP 848 (Figure 5.9).

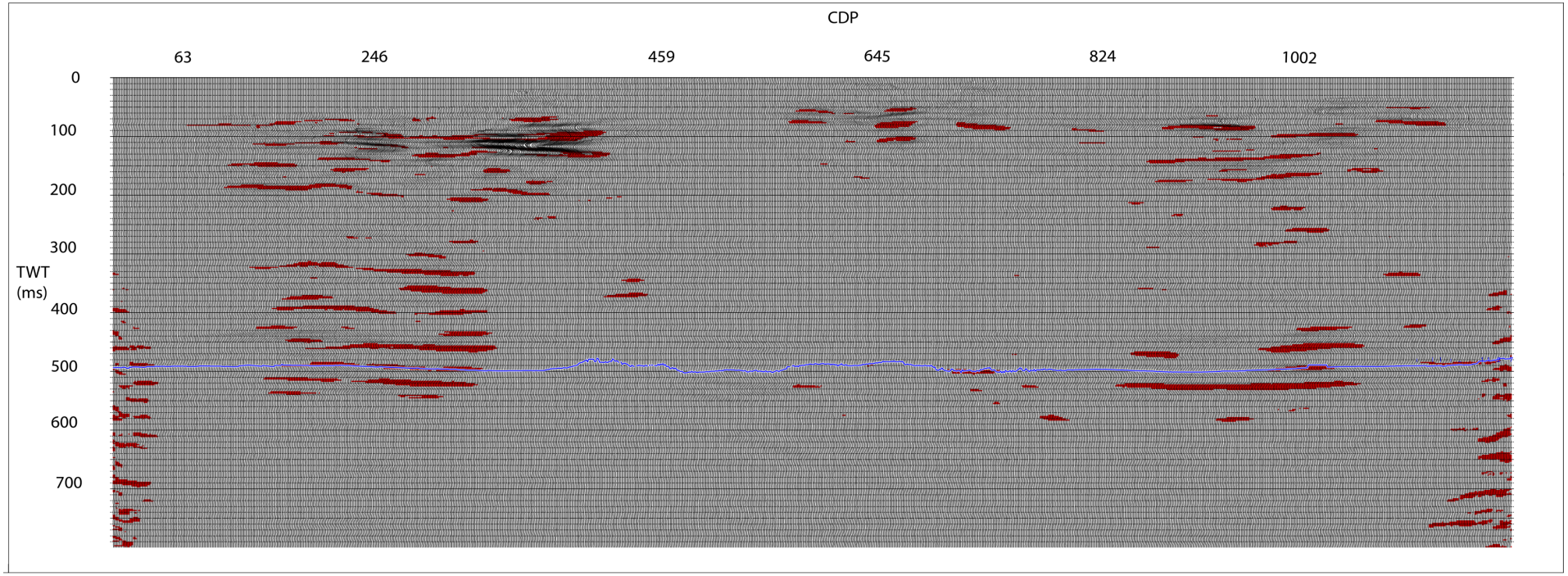

Figure 5.8. Line 101 AVO attribute volume. The data volume is the post-stack 2-D seismic reflection profile for line 101. The red zones indicate potential hydrocarbons throughout the seismic section. This study only focuses on the potential hydrocarbon layer within the Hartselle Sandstone (blue line).

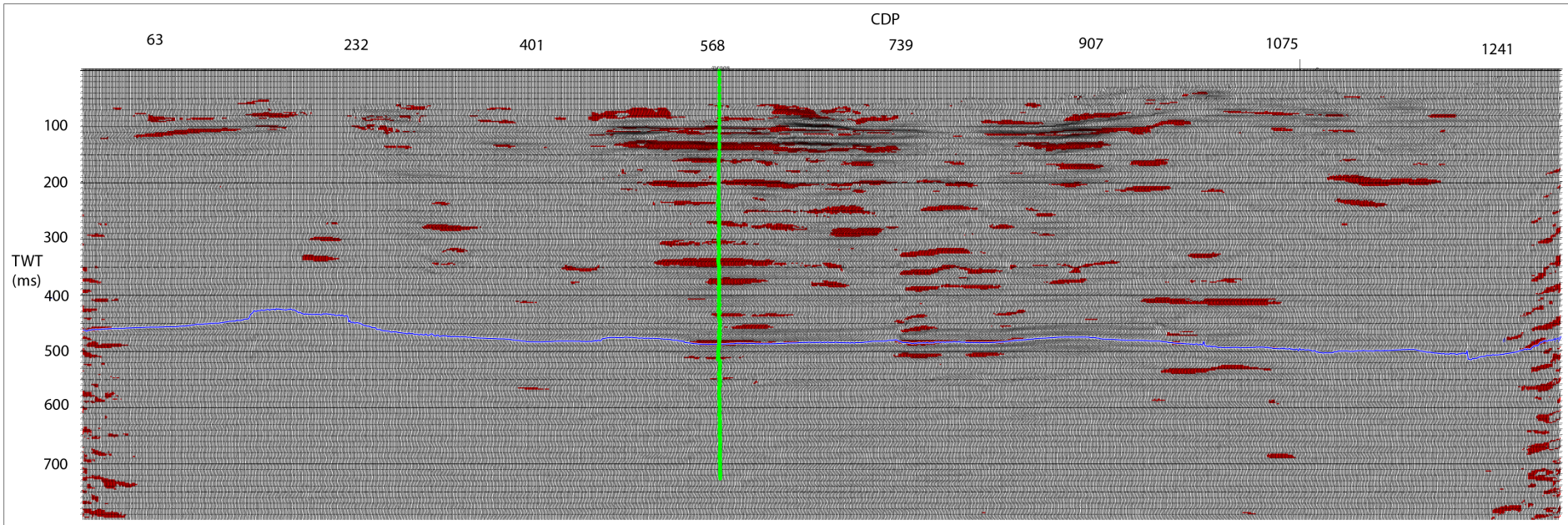

Figure 5.9. Line 201 AVO attribute volume. The data volume is the post-stack 2-D seismic reflection profile for line 201. The red zones indicate potential hydrocarbons throughout the seismic section. This study only focuses on the potential hydrocarbon layer within the Hartselle Sandstone (blue line). The green curve at CDP 576 indicates the location closest to the Gorgas #1 well.

The location of intercept and gradient values in the crossplot aids the interpretation of the AVO siliciclastic classification (Figure 5.10). Since hydrocarbons were found at the well and since CDP 576 from seismic line 201 is closest to the well, the AVO signature at this location aids in the AVO interpretation for potential hydrocarbons. An angle gather at CDP 576 within line 201, closest to the well, shows distinct variation in amplitude with increasing angle along the Hartselle Sandstone horizon (Figure 5.11).

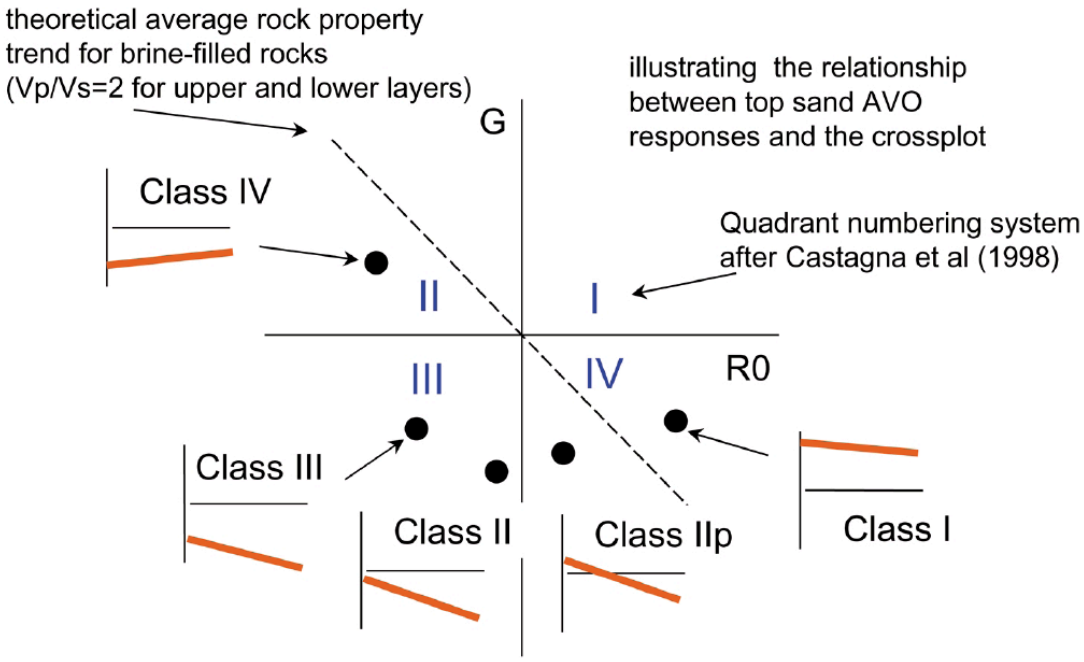

Figure 5.10. AVO classes and crossplot from Simm et al. (2000). G indicates the gradient and R0 indicates the intercept in the crossplot. Gradient curves (orange lines) associated with each AVO class are shown. Roman numerals indicate the quadrant numbering system after Castagna et al. (1998).

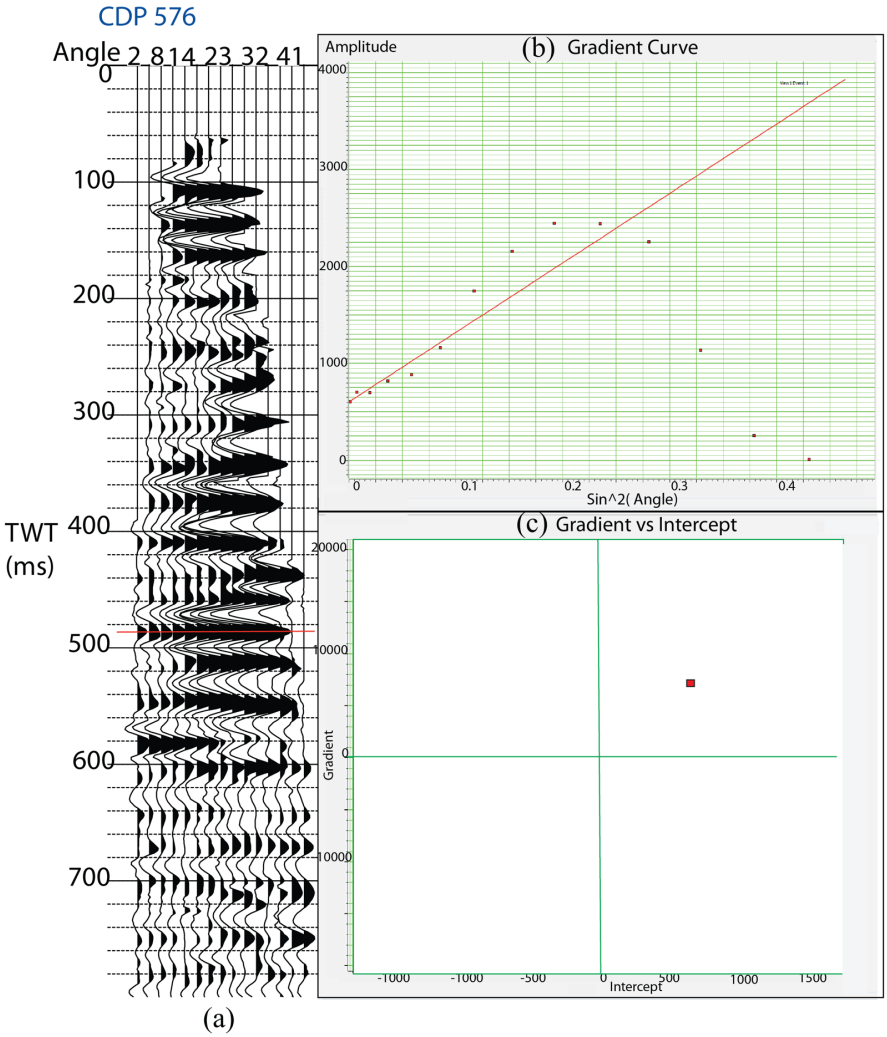

Figure 5.11. (a) Angle gather at CDP 576 (closest to the well) along line 201. The red line across the peak amplitude traces above 500 ms (TWT) indicates the Hartselle Sandstone horizon. (b) Gradient curve shows amplitude increasing from 0 - 0.2 $\sin^2(\theta)$ and decreasing from 0.2 to 0.4 $\sin^2(\theta)$. The Hartselle Sandstone intercept and gradient values plot within the first quadrant of the gradient versus intercept crossplot (c) of the reflections at this angle gather..

The gradient curve in Figure 5.11 indicates positive amplitude increasing over the first half of $\sin^2$(angle) but decreasing over the second half of $\sin^2$(angle). The intercept-gradient crossplot in Figure 5.11 includes the calculated intercept and gradient values for all reflectors throughout the angle gather at CDP 576. The intercept and gradient values of the Hartselle Sandstone at this angle gather were calculated and plotted in the first quadrant of the intercept-gradient crossplot (Figure 5.10; Figure 5.11). Similar gradient curves for an angle gather at CDP

70 within line 101 and an angle gather at CDP 500 within line 201, indicate positive amplitude decreasing with increasing angle (Figure 5.12). The intercept and gradient values of these gathers are both plotted in the fourth quadrant of the crossplots (Figure 5.12).

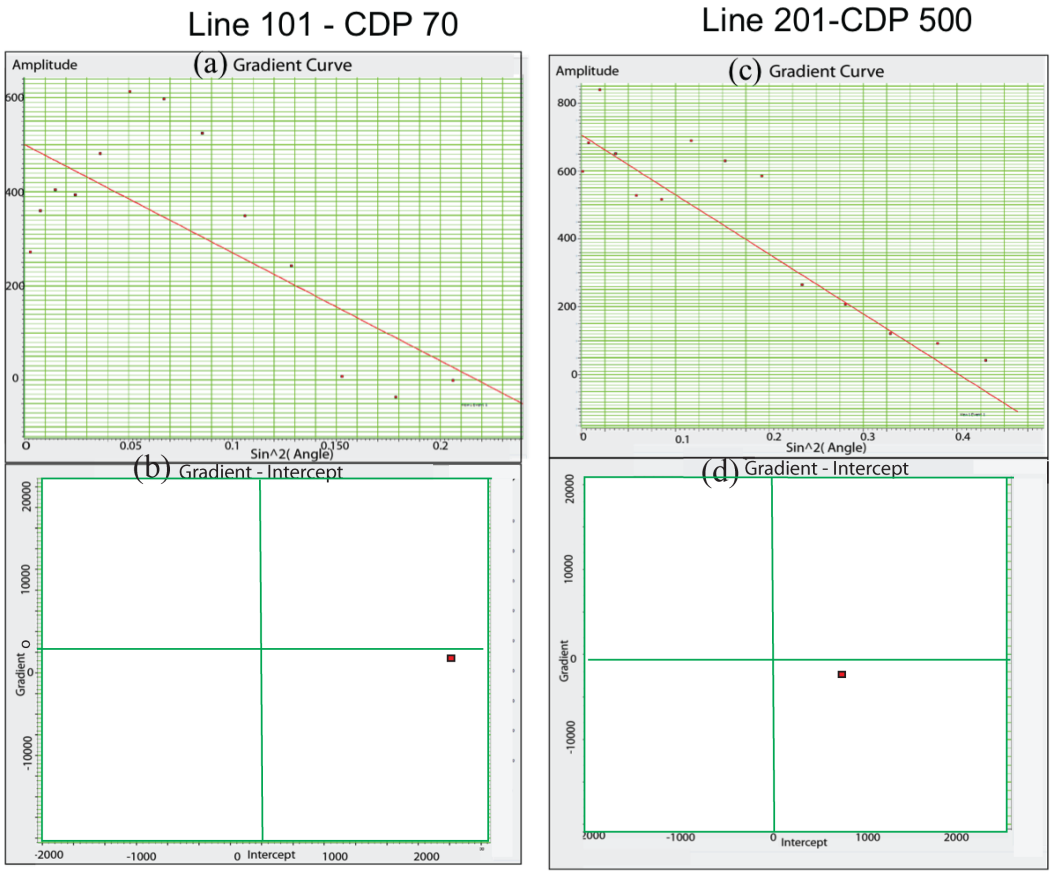

Figure 5.12. Gradient curve for the Hartselle Sandstone at CDP 70 of line 101 (a) shows the amplitude decreasing with $\sin^2(\theta)$. The Hartselle Sandstone intercept and gradient values, which are indicated by the red arrow, plot within the fourth quadrant of the gradient versus. intercept crossplot of the reflections at this angle gather (b). The gradient curve for the Hartselle SandstoneSanstone at CDP 500 of line 201 (c) shows the amplitude decreasing with $\sin^2(\theta)$. The Hartselle Sandstone intercept and gradient values, which are indicated by the red arrow, plot within the fourth quadrant of the gradient vs. intercept crossplot (d) for the reflections at this angle gather.

5.3.3 Forward Modeling Results

A pre-stack synthetic was generated to simulate the seismic characteristics at the well location (Figure 5.13). Results show that the synthetic model reflection events at the well location are similar to those recorded in the real seismic gather (CDP 576 angle gather from line

201); these reflections events have much stronger amplitudes than those of the real seismic gather. There are also amplitude variations throughout the synthetic gather. The AVO intercept-gradient analysis performed within the synthetic pre-stack angle gather shows positive amplitude increasing with increasing angle along the Hartselle Sandstone horizon (Figure 5.14). The intercept and gradient values for the synthetic angle gather along the Hartselle Sandstone horizon plot in the first quadrant of the intercept-gradient crossplot (Figure 5.14).

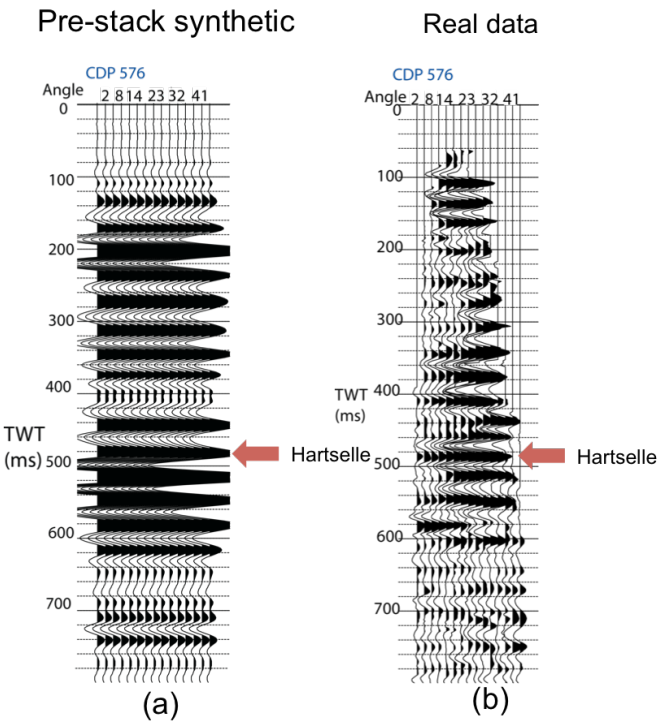

Figure 5.13. a) Pre-stack synthetic seismogram. (b) Angle gather at CDP 576 (closest to the well) from line 201.

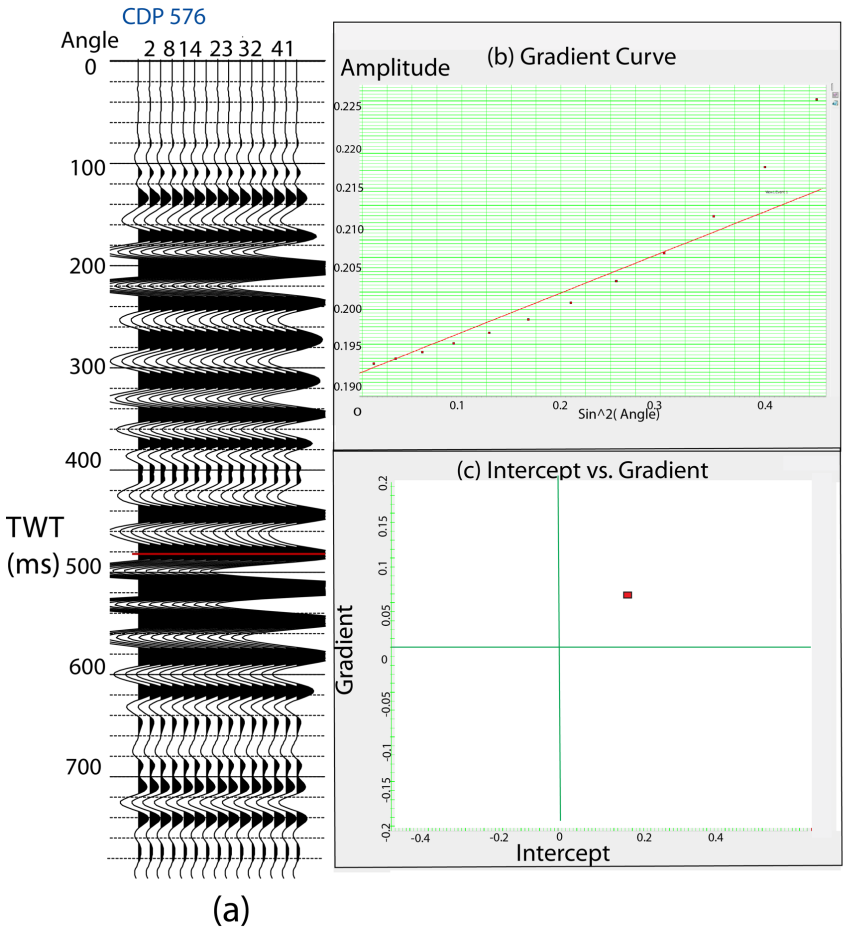

Figure 5.14. (a) Pre-stack synthetic seismogram. The red line across the peak amplitude traces above 500 ms (TWT) and indicates the Hartselle Sandstone horizon. The gradient curve in (b) shows the amplitude increasing with $\sin^2(\theta)$. The Hartselle Sandstone intercept and gradient values plot within the first quadrant of the gradient versus intercept crossplot (c) of the reflections at the synthetic.

The results from the fluid substitution (Figure 5.15) show three pre-stack synthetic seismograms that model the AVO effects of different scenarios of pure brine, pure oil, and pure gas sand in the reservoir zone. The intercept and gradient values for these synthetic seismograms also plot in the first quadrant of the intercept-gradient crossplots. Moreover, the intercept and gradient values for pure brine plot closer to the center of the crossplot, while those for pure oil and pure gas plot farther away from the center of the crossplot.

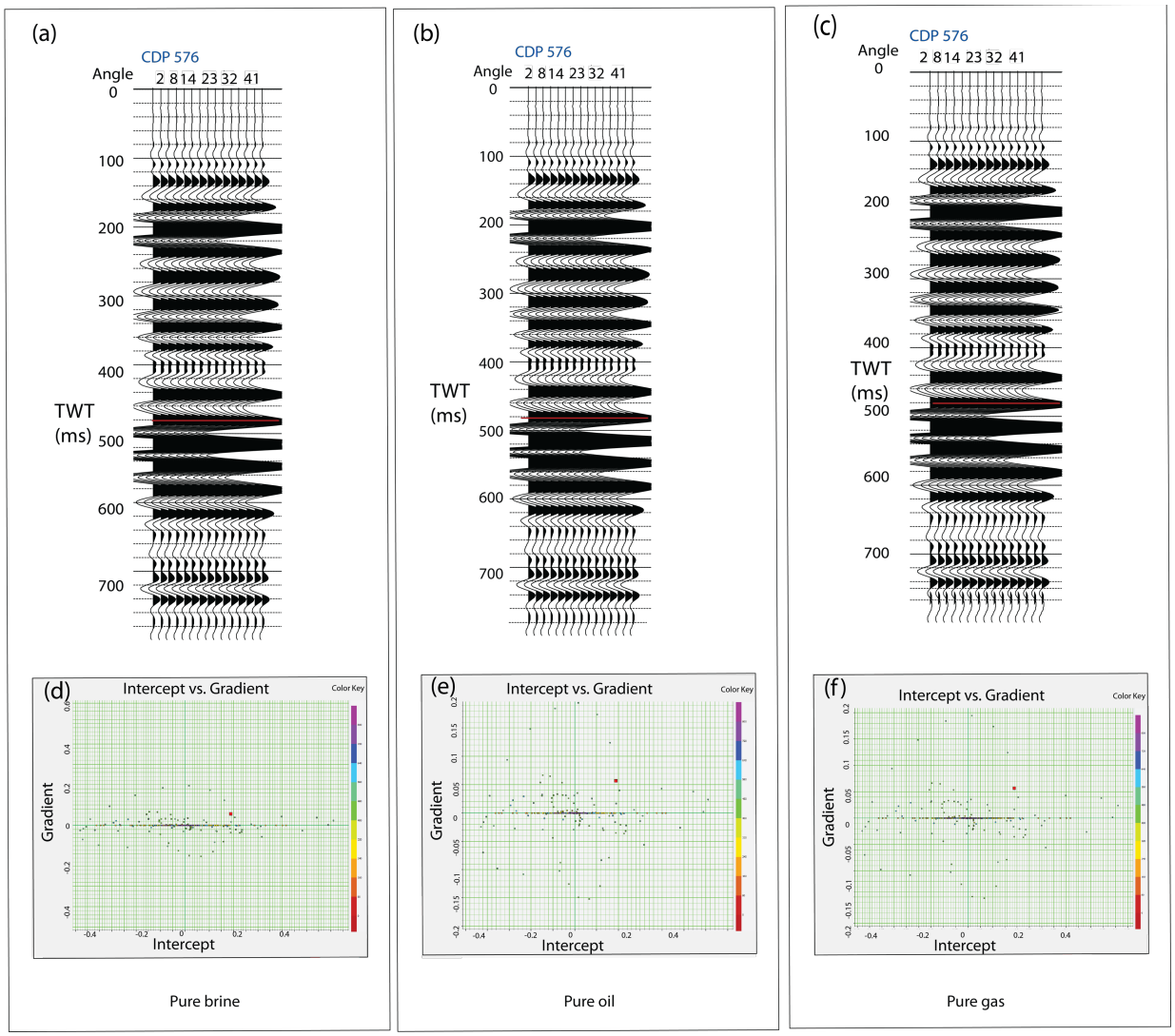

Figure 5.15. Pre-stack synthetic seismogram for a) pure brine sand, b) pure oil sand, c) pure gas sand, and their corresponding crossplots (d, e, and f). The Hartselle Sandstone intercept and gradient values for all three scenarios plot within the first quadrant of the gradient versus intercept crossplots.

5.3.4 Volumetric Analysis Results

The extent of the potential zone of hydrocarbons was estimated based on the AVO attribute volume results (Figure 5.8 and 5.9). Since the objective for this study is to evaluate the potential hydrocarbons within the Hartselle Sandstone, only the red zones in the seismic sections that coincide with the Hartselle Sandstone were evaluated. In the AVO attribute volume for line 101, the hydrocarbon layers within the Hartselle Sandstone extend a distance of 594 m (1948.82 ft) from CDP 16 to CDP 37 and from CDP 232 to CDP 310. In the AVO attribute volume for line 201, the hydrocarbon layer within the Hartselle Sandstone extends a distance of 1284 m (4212.60 ft) from CDP 548 to CDP 646 and from CDP 732 to CDP 848. The areal extent of the hydrocarbons along both seismic lines was estimated (Table 3). The mean estimate for line 101 is 0.2 km^2 (50 acres) and for line 201 is 0.5 km^2 (146 acres). These estimates were used as input for the volumetric and risking package.

Table 3
The Extent of Hydrocarbons Estimated in the Hartselle Sandstone within the Gorgas Area

Line 101				
P	distance (ft)	radius (ft)	area (ft^2)	area (Acres)
P10	1948.82	974.41	2.98E+6	73
Mean	1665.26	832.63	2.18E+6	50
P90	100	50	7.85E+3	0.2
Line 201				
P	distance (ft)	radius (ft)	area (ft^2)	area (acres)
P10	4212.6	2106.3	1.39E+7	320
Mean	2845.6	1422.8	6.36E+6	146
P90	800	400	5.03E+5	11

The volumetric analysis and risking follows a P10-large and P90-small convention, which means that P10 is a confident estimate and P90 is a conservative estimate. For example, in this P10-large and P90-small convention, P10 has a large numeric value such that there is a 10% chance of finding that value, whereas P90 has a small numeric value such that there is a 90%

chance of finding that value. P50 is a medium estimate with a 50% chance of finding that value. For this study, P10-large and P90-small is useful to indicate the predicted amount and the confidence level in achieving that amount. The Hartselle Sandstone reservoir parameters, including the areal extent of hydrocarbons along lines 101 and 201, core thickness, average porosity, and average hydrocarbons saturation, were input to the Rose and Associates multi-method risk analysis package (Table 4). The results provide an estimate of the volume of hydrocarbons in place (resources) for lines 101 and 201 and the chance of exceeding that amount (chance) (Figure 5.16, Figure 5.17). The results show that resources and chance are inversely proportional. In the volumetric and risk analysis for line 101 (Figure 5.16), there is a 32.4% chance of exceeding the minimum resources estimate of 0.5 mmbo (million barrels of oil). Since the amount estimated is low, the confidence in achieving this amount is high. At P90, there is a 29.2% chance of exceeding the small resources estimate of 0.8 mmbo. At P50, there is a 16.2% chance of exceeding the medium resources estimate of 1.4 mmbo. At mean or average resources, there is a 13.5% chance of exceeding 1.6 mmbo. Finally, at P10, there is a 3.2% chance of exceeding the large resources estimate of 2.5 mmbo.

Table 4
The Areal Extent of Hydrocarbons and the Reservoir Parameters of the Hartselle Sandstone in the Gorgas Area.

P	Line 101's Productive area (Acres)	Line 201's Productive area (Acres)	Interval thickness m (ft)	Average Porosity	Average Hydrocarbons Saturation	Oil Formation Volume Factor
P99	0	3	25.6 (84)	4.03	66.3	1.2704
P90	0	11	25.9 (85)	4.98	69.2	1.2733
Mode	4	12	26.1 (86)	6.22	76.5	1.2733
P50	4	63	26.1 (86)	6.35	77.1	1.285
Mean	50	146	26.1 (86)	6.42	77.2	1.285
P10	73	331	26.5(87)	7.97	85.2	1.2969
P01	801	1299	26.8 (88)	9.57	90	1.2998

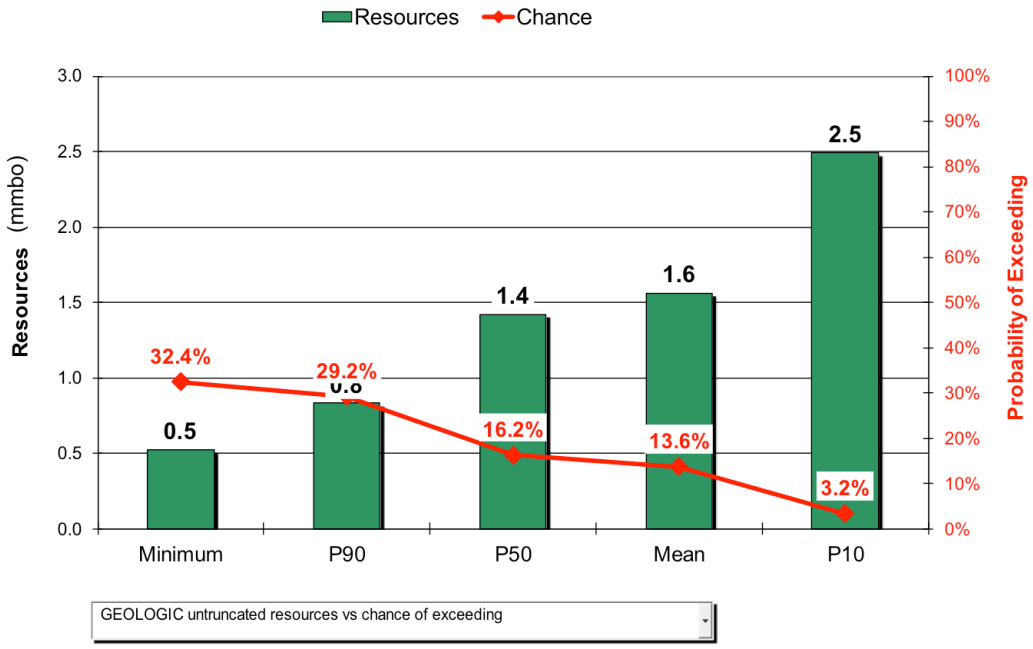

Figure 5.16. Resources versus chance chart for line 101. The green bars indicate the amount of estimated resources in million barrels of oil (mmbo) expected in the reservoir that are extractable. The red curve indicates the probability of exceeding that amount. The left-hand y-axis shows resources (mmbo), and the right-hand y-axis shows chance (%). The x-axis indicates the minimum (the minimum amount of resources estimated), P90, P50, mean (i.e., the mean values of the amount of resources estimated), and P10.

Similarly, the volumetric and risking analysis for line 201 (Figure 5.17) indicates there is a 32.4% chance of exceeding the minimum resources estimate of 0.1 mmbo. At P90, there is a 29.2% chance of exceeding the small resources estimate of 0.2 mmbo. At P50, there is a 16.2% chance of exceeding the medium resources estimate of 1.0 mmbo. At mean or average resources, there is a 13.5% chance of exceeding 2.3 mmbo. Finally, at P10, there is a 3.2% chance of exceeding the large resources estimate of 5.6 mmbo.

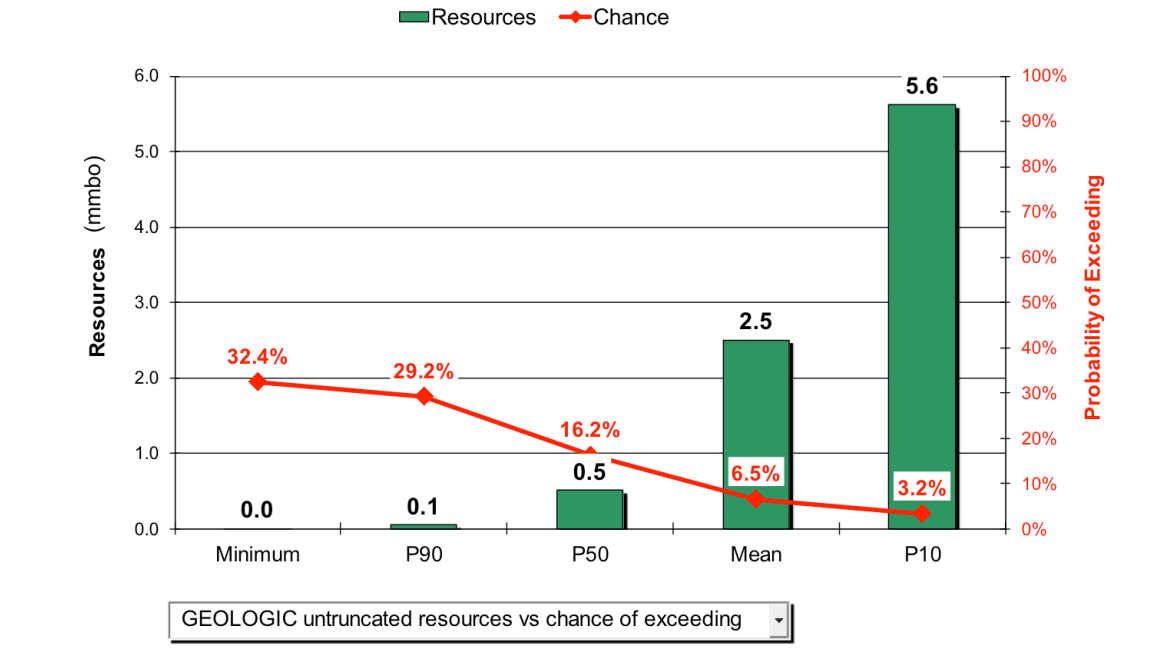

Figure 5.17. Resources vs. chance chart for line 201. The green bars indicate the amount of estimated resources in million barrels of oil (mmbo) expected in the reservoir that are extractable. The red curve indicates the probability of exceeding that amount. The left-hand y-axis shows resources (mmbo), and the right-hand y-axis shows chance (%). The x-axis indicates the minimum (the minimum amount of resources estimated), P90, P50 mean (i.e., the mean values of the amount of resources estimated), and P10.

CHAPTER 6: DISCUSSION

AVO is a useful method for the detection of hydrocarbons (Chiburis et al., 1993). However, AVO is not foolproof (Chopra and Castagna, 2014). The quality of seismic reflection data has a major influence on the results of the AVO calculations. As with other seismic reflection data collected on land, lines 101 and 201 have many limitations, including smearing in the stacks, statics, and resolution. A significant challenge with the seismic reflection processing, which was previously conducted by WesternGeco, was the many bends along lines 101 and 201. Because the sources and receivers were distributed along the meandering roads during the seismic reflection survey (Figure 1.4), the inability to focus the energy in one two-dimensional plane causes smearing in the stacks. Another issue is the statics, especially for line 101, which has significant elevation variations. While statics have been corrected during the seismic reflection processing, the center of line 101, coincident with the highest elevation (Figure 4.1), could still contain residual statics. Seismic conditioning for AVO performed in this study, specifically trim statics, deals with this problem by applying an optimal time shift to align the Hartselle Sandstone horizon throughout the seismic section. The resolution of the Hartselle Sandstone in the seismic reflection data is limited (45 m or 147.64 ft; Table 1), making the top and base of the unit unresolvable. Thus, the thickness of the Hartselle Sandstone unit cannot be interpreted from the seismic reflection data. However, the Hartselle Sandstone interval can still be detected. Thus, we know that despite being below seismic resolution, AVO analysis on the

Hartselle Sandstone was successful. The thickness of the Hartselle Interval is known to be 26 m (86 ft) in the Gorgas #1 core. The thickness of the Hartselle Sandstone unit is assumed to be relatively constant in the Gorgas area (Table 4) for the purpose of the volumetric and risk analysis. AVO analysis was able to detect the lateral extent of potential hydrocarbons. The percentage of hydrocarbons saturation in the Hartselle Sandstone in the Gorgas area was obtained from the Clark et al. (2013) core analysis of the Gorgas #1 core (section 2.2). For the volumetric and risk analysis, the oil saturation of the rock volume within the area of potential hydrocarbons is assumed to be similar to that of the Gorgas #1 core (e.g. the average oil saturation is 24%). Due to the low resolution of the seismic reflection data, the oil saturation within the Hartselle Sandstone in the Gorgas area was not predicted using AVO analysis.

The line 201 gradient curve for the angle gather at CDP 576 (closest to the well; Figure 5.11) exhibits positive amplitude increasing for the first half of $\sin^2(\theta)$, but decreasing with the second half of $\sin^2(\theta)$. The intercept and gradient values for this angle gather were plotted in the first quadrant of the crossplot. This AVO response is different from the other gradient curve examples (Figure 5.12). This could be due to the tuning effect of the sub-resolution Hartselle Sandstone horizon. Usually, AVO responses from the top of hydrocarbon-saturated sands are different than those from the base of hydrocarbon-saturated sands (Figure 6.1; Hampson and Russell, 2004). The AVO anomalies above the background trend correspond to the base of hydrocarbon-saturated sand, whereas AVO anomalies below the background trend correspond to the top of the hydrocarbon-saturated sand (Figure 3.2). The calculated intercept and gradient values were plotted above the background trend, either in the first quadrant (Figure 5.11; Figure 5.14) or the fourth quadrant (Figure 5.12) of the crossplots, which suggest that the AVO response corresponds to the base of the Hartselle Sandstone. Moreover, the AVO analysis of the synthetic

seismograms (Figure 5.14), shows similar AVO responses to those of the real seismic gather, which is the line 201 angle gather at CDP 576 (Figure 5.11). This further confirms the interpretation of the AVO analysis.

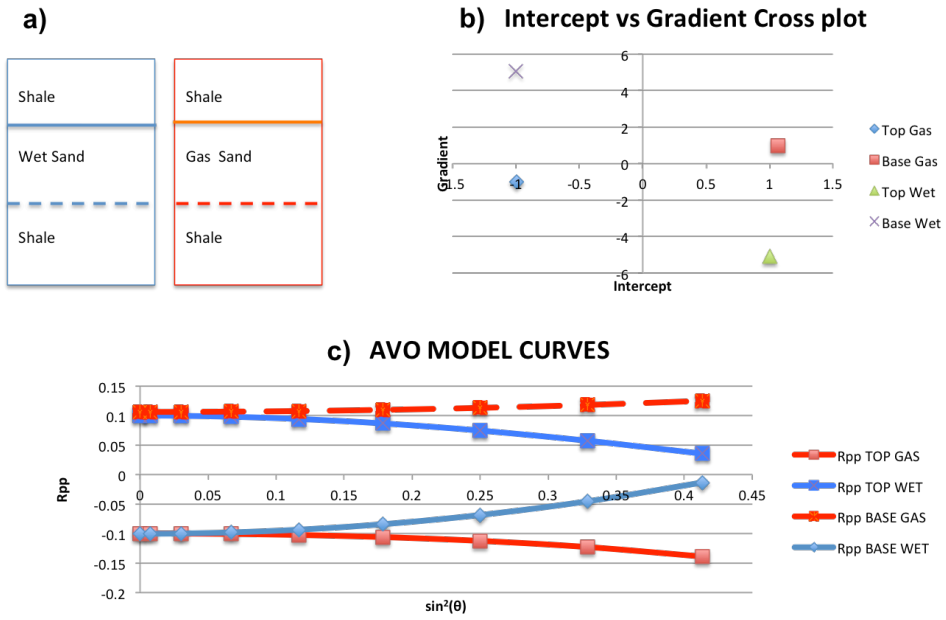

Figure 6.1 (a) 1-D lithology model- wet sand surrounded by shale versus gas sand surrounded by shale. Rpp on the y-axis indicates the amplitude. Intercept-gradient crossplot (b) and AVO model curves (c) for the 1-D lithology model were created using the Zoeppritz equations from Chopra and Castagna (2014), showing the different AVO responses from the top and bottom of gas sand, as well as from the top and bottom of wet sand. Adapted from Hampson and Russell (2004).

The background trend of the intercept-gradient crossplot corresponds to brine-saturated sand, while values in the crossplot that deviate from the background trend are considered AVO anomalies. The AVO crossplots show AVO anomalies that do not deviate very far from the fluid line and brine trend (Figure 5.6; Figure 5.7). This AVO anomaly zone is considered the potential zone for hydrocarbons within the Hartselle Sandstone horizon, which was mapped out with the attribute volumes for lines 101 and 201 (Figure 5.8; Figure 5.9). This zone is outlined only above the background trend of the AVO crossplots. This interpretation is based on the AVO responses of the Hartselle Sandstone from the AVO modeling (Figure 5.14; Figure 5.15) and from the real seismic reflection data near the well location where the light crude oil was found (Figure 11), which indicated AVO anomalies above the background trend (first quadrant of the crossplot). The potential zone of hydrocarbons extends outward from CDP 576 along line 201. Since this location is closest to the well, which contains hydrocarbons in the Hartselle Sandstone, the AVO anomalies detected in the seismic reflection data suggest the hydrocarbons layer extends beyond the well. This is a significant indication that AVO was able to detect hydrocarbons in the seismic reflection data around the Gorgas area. More anomalous AVO zones throughout the Hartselle Sandstone horizon were identified and measured to determine the lateral extent of this oil. The extent of the hydrocarbon layer within the Hartselle Sandstone along line 101 (594 m or 1948.82 ft) is less than half of that within the Hartselle Sandstone along line 201 (1284 m or 4212 ft). Thus, the total volume of oil estimated for line 101 is less than that for line 201 (Table 4; Figure 5.16; Figure 5.17). The reason for this could be that the line 101, which is perpendicular to line 201, extends farther away from the oil discovered in the Gorgas #1 well. Moreover, the lower quality of the seismic reflection data for line 101 may have affected the AVO results.

Intercept-gradient analyses for seismic lines 101 and 201 show positive amplitude decreasing with larger offsets, indicating an AVO class I (Figure 5.12). According to the AVO classification for siliciclastic sands, AVO class I corresponds to high impedance gas/oil sands (Castagna, 1998). From the velocity information acquired from the seismic reflection data and the density from the well logs, the Hartselle Sandstone is indeed higher impedance than the surrounding limestone (Table 5).

The resources versus chance charts produced from the volumetric and risk analysis for both line 101 and 201 (Figure 5.16; Figure 5.17) indicate a potentially significant amount of oil in the Gorgas area. With the natural fractures in place acting as secondary porosity, this volume could be larger. Tight oil extraction technology that is available today could unlock this resource. However, even though the volume and risk analysis indicates that there is a chance (3.2 to 32.4%) to unlock this oil resource (up to 0.5-5.6 mmbo) in the Gorgas area, with the current low price of oil, extraction and operation would not be economical considering the cost of building infrastructure for this prospect. Nevertheless, the seismic reflection data provide great insights on the subsurface resources and structure in this area. The AVO analysis from this study provides an estimate on the lateral extent of hydrocarbons within the Hartselle Sandstone. Knowing where the oil resources are located and the estimate of the total hydrocarbons in place provides information about the Hartselle Sandstone subsurface reservoir that can be valuable for future development of this oil resource in the future. Since drilling is costly (approximately $2-3 million), an AVO analysis of available pre-stack seismic reflection data is an economical technique to help interpreters and investors make a more informed decision on where to drill and prevent the drilling of dry holes. However, AVO, like many geophysical techniques, still has major challenges and uncertainties. There are multiple factors, such as the quality of the seismic

reflection data, imaging problems, poor velocity models, and structural effects, which may alter the AVO results. Thus, careful processing of the seismic reflection data and the application of a new velocity model during the migration process for both seismic lines (beyond the scope of this study), is recommended for future studies to enhance the quality of the data for better AVO results. Oil and gas saturations of the Hartselle Sandstone may be better predicted from the seismic reflection data by creating models of different scenarios of fluid saturation (percent oil, percent gas, and percent brine) and comparing those models with the seismic reflection data.

The Cretaceous Bluesky Sandstone reservoir along the Alberta/British Columbia border in Canada is an analog for the Hartselle Sandstone. The Bluesky Sandstone is encountered at a depth of 1000 m (3280.84 ft; Downton, 1997).). it is also considered an AVO class I high impedance oil sand (Downton, 1997). As the largest oil sand deposits in North America, oil sands in Alberta, Canada, have a long history of exploration and development and are comparable with the oil sands in Alabama (Hills et al., 2016). The Hartselle Sandstone is encountered at a depth of 797 m (2615 ft) in the Gorgas #1 borehole. The Hartselle Sandstone is known to be the third largest oil sand resource in the US (Wilson, 1987). Unlike Alberta's oil sands, there currently has been no commercial exploitation of the oil resource of the Hartselle Sandstone. However, the potential of the Hartselle Sandstone could be significant (Hills et al., 2016). The level of interest in the development and operation of the Hartselle Sandstone is driven by economic and technical factors (Hills et al., 2016). The Alabama Oil Sands Program (AOSP) has been established by the Oil and Gas Board of the Geological Survey of Alabama to further investigate the potential of the Hartselle Sandstone (Hills et al., 2016). Assuming favourable economic conditions (such as when the price of oil is high), development including either surface or subsurface operations might occur depending on the thickness, grade, extent, topography,

overburden, water availability, transportation routes, and potential adverse environmental and socioeconomic effects (Hills et al., 2016).

CHAPTER 7: CONCLUSIONS

1) This thesis explores the applicability of the AVO process to characterize the Hartselle Sandstone reservoir in the vicinity of Gorgas Power Plant. Using AVO, a geophysical technique for the direct detection of hydrocarbons, the lateral extent of the hydrocarbon resource was successfully estimated.

2) AVO is not a foolproof method. The quality of the Vibroseis seismic reflection data has limitations including smearing, statics, and resolution. Seismic conditioning was performed to further enhance the data for the AVO analysis. Although the seismic reflection data have a limited resolution; the Hartselle Sandstone unit, with a thickness of 26 m (86ft), can still be detected.

3) AVO responses from the top of hydrocarbon-saturated sands are different from those from the base of hydrocarbon-saturated sands. The line 201 gradient curves for the angle gather at CDP 576 (closest to the well) has a different AVO response than the other gradient curve examples. This could be due to the tuning effect of the sub-resolution of the Hartselle Sandstone horizon.

4) The AVO analysis along the Hartselle Sandstone from the seismic reflection data show a pattern of positive amplitude decreasing with larger offsets. This indicates a class I AVO anomaly, which is a typical high impedance hydrocarbon-saturated sand.

5) Intercept-gradient crossplots are useful for the interpretation of the AVO anomalies. Anomalous AVO values were interpreted from the crossplots as potential zones of hydrocarbons, which were then mapped across both seismic reflection profiles. These zones were observed to extend outward from the CDP 576 of line 201, coincident to the closest location to the well where the oil resource was discovered. This indicates the feasibility of AVO application to the subsurface data from the Gorgas area.

6) The lateral extent of hydrocarbons within the Hartselle Sandstone along line 101 (594 m or 1948.82 ft) is estimated to be less than half of that within the Hartselle Sandstone of line 201 (1284 m or 4212 ft). The mean estimate of the areal extent of hydrocarbons for the line 101 is 0.2 km^2 (50 acres) and for line 201 is 0.5 km^2 (146 acres). Volumetric and risk analysis of the potential hydrocarbons in the Hartselle Sandstone indicates that this area has a large resource potential, with an estimated total volume of hydrocarbons in place ranging from 0.1-5.6 mmbo. For line 101, there is a 13.5% chance of exceeding the mean estimate of the amount of hydrocarbons in place of 0.8 mmbo. For line 201, there is a 13.5% chance of exceeding the mean estimate of the amount of hydrocarbons in place of 2.3 mmbo.

7) The total volume of oil estimated for line 101 is less than that for line 201. The reason for this could be that line 101 is perpendicular to line 201 and extends farther away from the oil discovered in the Gorgas #1 well. Moreover, the lower quality of the seismic reflection data along line 101 may have affected the AVO results.

8) Further seismic processing (beyond the scope of this study) may improve the AVO results. This includes a better statics correction and migration with a better velocity model to remove the NMO effects and horizontally align the seismic reflections.

9) Since the Hartselle Sandstone is a tight oil prospect, tight oil extraction technology would be necessary to unlock this resource. Under the current low oil price, operation in this area is uneconomical considering the high cost of tight oil extraction.

10) Since drilling dry holes is problematic and costly, an investigation of available pre-stack seismic reflection data is an ideal way (that can save time and money) to make an informed decision on where to drill. The AVO analysis conducted in this study will contribute to the understanding of the Hartselle Sandstone reservoir in this area, which could be valuable for future development of this resource.

REFERENCES

Avseth, P., Janke, A. and Horn, F. (2016). AVO inversion in exploration — Key learnings from a Norwegian Sea prospect. *The Leading Edge*, 35(5), 405-414, doi:10.1190/tle35050405.1.

Carroll, R.E., Pashin, J.C. and Kugler, R.L. (1995). Burial history and source-rock characteristics of Upper Devonian through Pennsylvanian strata, Black Warrior Basin, Alabama. *Geological Survey of Alabama Circular*, 187, 29.

Castagna, J. (1993). AVO Analysis —Tutorial and Review, in Offset-dependent Reflectivity Theory and Practice of AVO Analysis, Castagna, J. P. and Backus, M, M (eds.), *SEG Investigations in Geophysics 8* (pp. 57-77). Tulsa, OK: Society of Exploration Geophysicists.

Castagna, J. P., Swan, H. W. and Foster, D. J. (1998). Framework for AVO gradient and intercept interpretation. *Geophysics*, 63(3), 948, doi:10.1190/1.1444406.

Chiburis, E. (1993). AVO Applications in Saudi Arabia, in Offset-dependent Reflectivity Theory and Practice of AVO Analysis, Castagna, J. P. and Backus, M, M (eds.), *SEG Investigations in Geophysics 8* (pp. 211-237). Tulsa, OK: Society of Exploration Geophysicists.

Chiburis, E., Leaney, S., and Skidmore, C. (1993). Hydrocarbon Detection with AVO. *Oilfield Review*, 5, 1-9.

Chopra, S. and J. Castagna (2014). AVO. *SEG Investigations in Geophysics 16*. Tulsa, OK: Society of Exploration Geophysicists.

Clark, P., Pashin, J., Carlson, E., Goodliffe, A., McIntyre-Redden, M., Mann, S., and Thompson M. (2013). Site Characterization for CO_2 Storage from Coal-fired Power Facilities in the Black Warrior Basin of Alabama, United States. USDOE.

Cleaves, A.W. and Stapor, F.W. (1992). Mississippian (Chesterian) Sequence Stratigraphy in the Black Warrior Basin: Pride Mountain Formation (Lowstand Wedge) and Hartselle SandstoneHartselle Sandstone (Transgressive Systems Tract). *Gulf Coast Association of Geological Societies Transactions*, 42, 683-696.

Dey-Sarkar, S. K. and Svatek, S.V. (1993). Prestack analysis: An integrated approach for seismic interpretation in clastic basins, in Offset-dependent Reflectivity Theory and Practice of AVO Analysis, Castagna, J. P. and Backus, M, M (eds.), *SEG Investigations in Geophysics 8* (pp. 57-77). Tulsa, OK: Society of Exploration Geophysicists.

Downton, J. (1997). AVO Attribute Analysis on a Class I Clastic Reservoir, Recorder, 22, 1-7.

Estill, R. and Wolstad, K. (1993). Interpretive aspects of AVO application to offshore Gilf Coast bright-spot analysis, in Offset-dependent Reflectivity Theory and Practice of AVO Analysis, Castagna, J. P. and Backus, M, M (eds.), *SEG Investigations in Geophysics 8* (pp. 267-284). Tulsa, OK: Society of Exploration Geophysicists.

Fadolalkarem, Y. (2015). Pre-stack Seismic Attribute Analysis of the Mississippian Chert and the Arbuckle Group at the Wellington Field, South-central Kansas, M.S. thesis, Dep. of Geology, Univ. of Kansas, Lawrence, KS.

Foster, D. J. and Keys, R.G. (1999). Interpreting AVO responses. *SEG Technical Program Expanded Abstracts,* 18(1). 748, doi:10.1190/1.1821135.

Gregory, A. R. (1977). Aspects of rock physics from laboratory and log data that are important to seismic interpretation, in Seismic Stratigraphy — Applications to Hydrocarbon Exploration, Payton, C. E. (ed.), *AAPG Memoir 26*, 15–46.

Groshong, R. H., J. C. Pashin, and M. R. McIntyre (2009). Structural controls on fractured coal reservoirs in the southern Appalachian Black Warrior foreland basin. *Journal of structural geology*, 31, 874–886, doi:10.1016/j.jsg.2008.02.017.

Hampson, D. (2004). Trim Statics in Hampson-Russell software *In* the knowledge base of the Hampson-Russell software. Hampson-Russell Calgary Office (November 2008)

Hampson, D. and Russell, B. (2004). AVO theory. Retrieved on 26.06.2017 from ftp://ftp.hampson-russell.com/pub/manuals/avo_theory.pdf

Hampson, D. and Russell, B. (2007). AVO guide *In* the knowledge base of the Hampson-Russell software. Hampson-Russell Calgary Office (November 2007)

Hills, D.J., Hooks, C.H., McIntyre-Redden, M.R., Crooke, L.A., Tew, B.H., Jr., and Parks, K. (2016). Oil sands in Alabama, USA: A fresh look at an emerging potential resource. *Bulletin of Canadian Petroleum Geology*, 64, 278–290, doi:10.2113/gscpgbull.64.2.278.

Hong, M.R., Castagna, J. P., Sicking, C. J. (1993). A Model-Based Analysis of AVO in the Sacramento Valley in Offset-dependent Reflectivity Theory and Practice of AVO Analysis, Castagna, J. P. and Backus, M, M (eds.), *SEG Investigations in Geophysics 8* (pp. 130-137). Tulsa, OK: Society of Exploration Geophysicists.

Hooks, C., D. Hills, and M. McIntyre-Redden, M. (2016). The Hartselle SandstoneHartselle Sandstone, Alabama's Oil Sands Resource, paper presented at AAPG Annual Convention and Exhibition, Calgary, Alberta, Canada.

Koefoed, O. (1955). On the Effect of Poisson's Ratios of Rock Strata on the Reflection Coefficients of Plane Waves. Geophysical Prospecting, 3(4), 381-387, doi:10.1111/j.1365-2478.1955.tb01383.x.

Mavko, G., Chan, C., and Mukerji, T. (1995). Fluid substitution: Estimating changes in V_P without knowing V_S. *Geophysics*, 60 (6), 1750-1755.

Ostrander, W. J. (1984). Plane-wave reflection coefficients for gas sands at nonnormal angles of incidence. *Geophysics*, 49(10). 1637, doi:10.1190/1.1441571.

Pashin, J. C. and Raymond, D. E. (2004). Glacial-eustatic control of coalbed methane reservoir distribution (Pottsville Formation; Lower Pennsylvanian) in the Black Warrior Basin of Alabama, 2004 Interntational Coalbed Methane Symp. Proc., Univ. Alabama, Tuscaloosa, paper 413,15.

Pashin, J. C., 1994. Cycles and stacking patterns in Carboniferous rocks of the Black Warrior foreland basin: *Transaction of the Gulf Coast Association of Societies*, 44,555-563.

Pashin, J. C., Grace, R. L. B., and Kopaska-Merkel, D. C. (2010). Devonian shale plays in the Black Warrior basin and Appalachian thrust belt of Alabama: Tuscaloosa, Alabama, University of Alabama, College of Continuing Studies, 2010 International Coalbed & Shale Gas Symposium Proceedings, paper 1016, 20.

Pawlewicz, M. J. and Hatch, J. R. (2007). Petroleum assessment of the Chattanooga Shale/Floyd Shale–Paleozoic Total Petroleum System, Black Warrior Basin, Alabama and Mississippi, *in* Hatch, Joseph R., and Pawlewicz, Mark J., compilers, Geologic assessment of undiscovered oil and gas resources of the Black Warrior Basin Province, Alabama and Mississippi: *U.S. Geological Survey Digital Data Series DDS–69–I*, 3, 23.

Robinson, D., Bailey R., and Goodliffe, A. (2012). Structure of The Alleghanian Thrust Belt under The Gulf Coastal Plain of Alabama. *GCAGS Journal*, 1, 44-54.

Rose, P.R. (2001). Risk Analysis and Management of Petroleum Exploration Ventures: *AAPG Methods in Exploration no. 12*.

Rutter, R. S. (2012). A geophysical characterization of stratigraphy in the eastern Black Warrior Basin underlying Gorgas Power Generation Plant, Walker County, Alabama, M.A. thesis, Dep. of Geological Sciences, Univ. of Alabama, Tuscaloosa, AL.

Ryder, R. T. (1987). Oil and Gas Resources of the Black Warrior Basin, Alabama and Mississippi:: *U. S. Geological Survey*, report 87-450X, 25.

Simm, R., White, R. White, and Uden, R. Uden (2000). The anatomy of AVO crossplots. *The Leading Edge, 19(2)*. 150, doi:10.1190/1.1438557.

Stommel, H.E., and Graul, J. M. (1978). Current trends in geophysics: 7th Annual Convention Proceedings., Indonesian Petroleum Association, 133-158.

Swan, H. W. (1993). Properties of direct AVO hydrocarbon indicators, in Offset-dependent Reflectivity Theory and Practice of AVO Analysis, Castagna, J. P. and Backus, M, M (eds.), *SEG Investigations in Geophysics 8* (pp. 78-92). Tulsa, OK: Society of Exploration Geophysicists.

Thomas, W. A. (1974). Converging clastic wedges in the Mississippian of Alabama: *Geological Society of America Special Paper,* 148,187-207.

Thomas, W. A. (1985). The Appalachian-Ouachita connection: Paleozoic orogenic belt at the southern margin of North America: *Annual Review of Earth and Planetary Sciences*, 13, 175-199.

Thomas, W. A. (2007). Role of the Birmingham basement fault in thin-skinned thrusting of the Birmingham anticlinorium, Appalachian thrust belt in Alabama, *American Journal of Science*, 307, 42-62.

Thomas, W.A. (1985). The Appalachian-Ouachita Connection: Paleozoic Orogenic Belt at the Southern Margin of North America: *Annual Review of Earth and Planetary Sciences*, 13, 175-199, doi: 10.1146/annurev.ea.13.050185.001135.

Thomas, W.A. (1988). The Black Warrior Basin, *in* Sloss, L.L., ed., Sedimentary cover – North American craton: Boulder, Colorado, *Geological Society of America*, The Geology of North America, D-2, 471-492.

Thomas, W.A., and Mack, G. H, (1982). Paleogeographic relationship of a Mississippian barrier-island and shelf-bar system (Hartselle SandstoneHartselle Sandstone) in Alabama to the Appalachian-Ouachita orogenic belt. *Geological Society of America Bulletin*, 93, 6-19.

Thomas, W.A., and Whiting, B. M. (1994). Three-dimensional controls on subsidence of a foreland basin associated with a thrust-belt recess: Black Warrior basin, Alabama and Mississippi. *Geology*, 22, 727-730.

Wilson, G.V. (1987). Characteristics and resource evaluation of the asphalt and bitumen deposits of northern Alabama. *Geological Survey of Alabama Bulletin*, 111, 109.

Wood, J. R. (1984). A model for porosity reduction by quartz cementation in anticlinal structures: Abstract. *CDPG Special Publication*, 566.

Yilmaz, O. (2001). Seismic data analysis: processing, inversion, and interpretation of seismic data. *SEG Investigations in Geophysics 10*. Tulsa, OK: Society of Exploration Geophysicists.

Zoeppritz, K. (1914). On the Reflection and Transmission of Seismic Waves at Surfaces of Discontinuity, in Classics of Elastic Wave Theory. *SEG Geophysics Reprint Series No. 24* (pp. 363-376). Tulsa, OK: Society of Exploration Geophysicists.

APPENDIX I

GORGAS 2-D Processing Workflow by WesternGeco. Adapted from Rutter (2012).

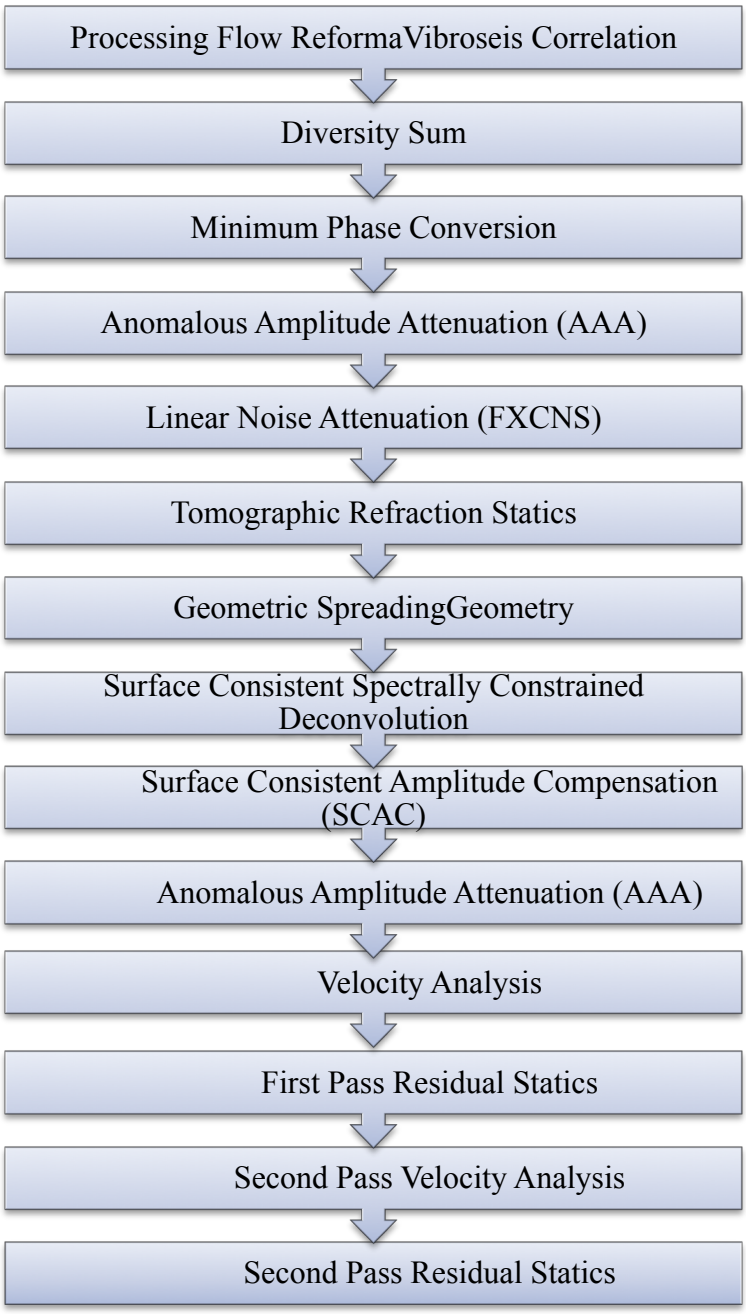

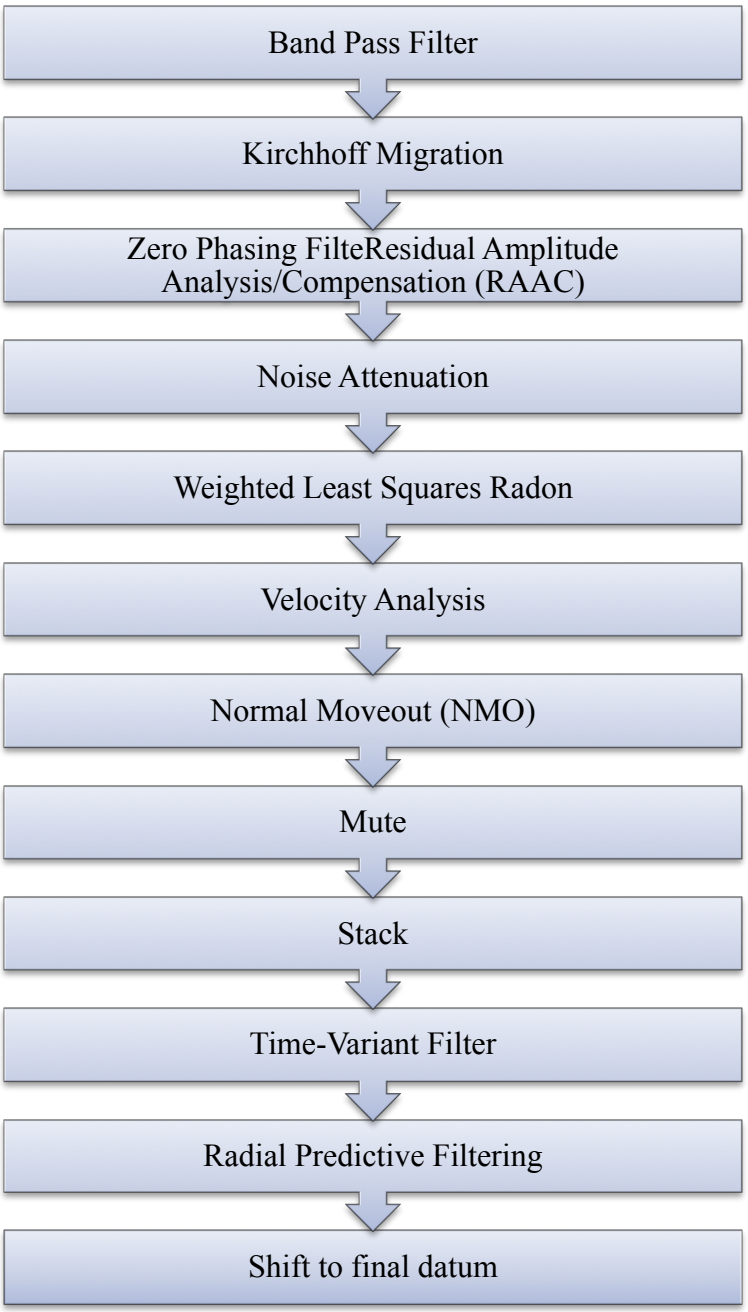
Band Pass Filter
Kirchhoff Migration
Zero Phasing FilteResidual Amplitude Analysis/Compensation (RAAC)
Noise Attenuation
Weighted Least Squares Radon
Velocity Analysis
Normal Moveout (NMO)
Mute
Stack
Time-Variant Filter
Radial Predictive Filtering
Shift to final datum

APPENDIX II

The formation tops, V_p, density, and V_s logs. TWT (ms) is displayed on the vertical axis on the left and MD (ft) from KB is indicated on the vertical axis on the right. The Hartselle Sandstone interval is highlighted in red within the formation tops column.

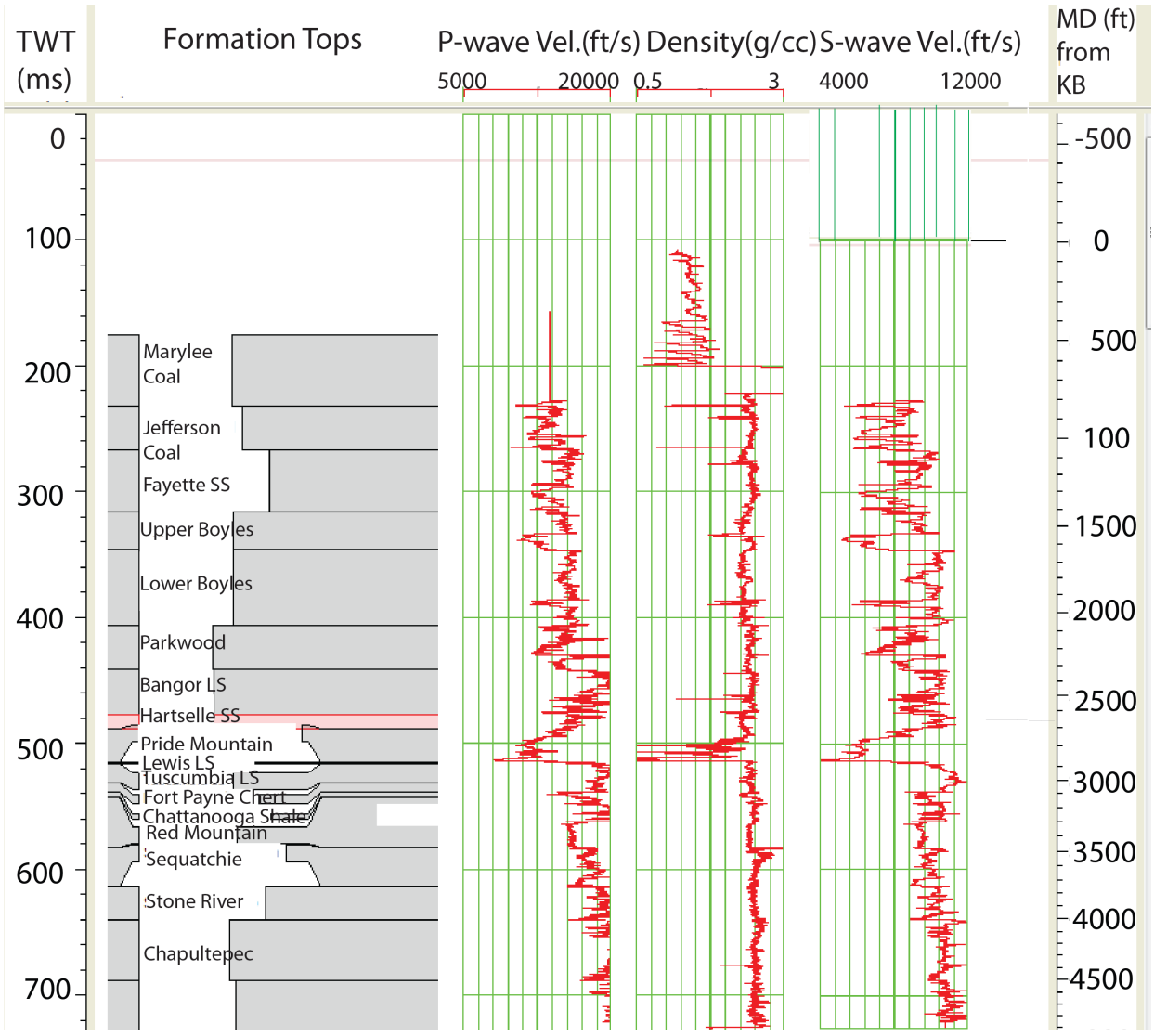

APPENDIX III

Check-shot Report: SRD = Seismic Reference Datum, OWT = One way time, KB = Kelly Bushing, RMS = Root mean squared. Adapted from Rutter (2012).

LEVEL	**VERTICAL**	**MEASURED**	**OBSERVED**	**VERTICAL**	**ACOUSTIC**	**ACOUSTIC**
NUMBER	DEPTH	DEPTH	TRAVEL	TRANSIT	AVERAGE	RMS
FROM	FROM	KB	TIME	TIME-SRD	VELOCITY	VELOCITY
SRD	(owt)	(owt)				
ft	ft	s	s	ft/s	ft/s	ft/s
1	0	-484	0			
2	833.9	349.9	0.0517	0.0798	10456	10456
3	883.9	399.9	0.0546	0.0835	10585	10602
4	933.9	449.9	0.0582	0.0877	10648	10667
5	984	500	0.0619	0.0919	10709	10731
6	1034	550	0.0656	0.096	10776	10801
7	1084	600	0.0689	0.0995	10893	10934
8	1134	650	0.0724	0.1033	10974	11021
9	1184	700	0.0759	0.107	11069	11126
10	1234	750	0.0799	0.1112	11100	11156
11	1284	800	0.0838	0.1152	11148	11205
12	1334	850	0.0878	0.1193	11180	11235
13	1384	900	0.0914	0.123	11252	11314
14	1434	950	0.0951	0.1268	11306	11369
15	1483.9	999.9	0.0989	0.1307	11351	11415
16	1533.9	1049.9	0.1027	0.1346	11392	11456
17	1583.9	1099.9	0.1063	0.1383	11455	11524
18	1633.9	1149.9	0.1097	0.1418	11524	11599

19	1683.9	1199.9	0.1132	0.1453	11590	11669
20	1733.9	1249.9	0.1165	0.1486	11664	11752
21	1783.9	1299.9	0.12	0.1522	11719	11810
22	1833.9	1349.9	0.1235	0.1557	11776	11871
23	1883.8	1399.8	0.1271	0.1593	11823	11919
24	1933.8	1449.8	0.1306	0.1629	11868	11965
25	1983.8	1499.8	0.1342	0.1665	11913	12012
26	2033.8	1549.8	0.1379	0.1703	11942	12039
27	2083.9	1599.9	0.1416	0.174	11978	12076
28	2133.9	1649.9	0.1452	0.1776	12015	12113
29	2183.9	1699.9	0.1485	0.181	12068	12170
30	2233.9	1749.9	0.1518	0.1842	12126	12233
31	2284.1	1800.1	0.1548	0.1873	12192	12308
32	2334.1	1850.1	0.1582	0.1907	12241	12359
33	2384.1	1900.1	0.1612	0.1938	12303	12428
34	2434.1	1950.1	0.1646	0.1972	12343	12469
35	2483.5	1999.5	0.168	0.2005	12384	12512
36	2533.5	2049.5	0.1713	0.2039	12423	12553
37	2583.5	2099.5	0.1748	0.2075	12453	12582
38	2633.5	2149.5	0.1779	0.2106	12508	12642
39	2683.8	2199.8	0.1816	0.2142	12528	12660
40	2733.8	2249.8	0.1847	0.2174	12577	12714
41	2784.1	2300.1	0.1882	0.2209	12605	12741
42	2834.1	2350.1	0.1911	0.2238	12665	12810
43	2884.1	2400.1	0.194	0.2267	12723	12875
44	2934.1	2450.1	0.1965	0.2292	12799	12969
45	2984	2500	0.1993	0.232	12860	13039

46	3033.8	2549.8	0.2022	0.2349	12916	13101
47	3084	2600	0.2053	0.238	12959	13147
48	3134	2650	0.2082	0.241	13006	13197
49	3184	2700	0.2115	0.2442	13036	13227
50	3234	2750	0.2146	0.2474	13074	13266
51	3269.1	2785.1	0.217	0.2498	13088	13278
52	3384	2900	0.2263	0.2591	13061	13246
53	3434	2950	0.2293	0.2621	13104	13292
54	3484	3000	0.232	0.2648	13157	13352
55	3534	3050	0.2346	0.2674	13218	13425
56	3584	3100	0.2373	0.2701	13267	13480
57	3634	3150	0.24	0.2728	13323	13545
58	3684	3200	0.2429	0.2758	13359	13583
59	3734	3250	0.2456	0.2784	13411	13641
60	3783.9	3299.9	0.2484	0.2813	13453	13686
61	3833.9	3349.9	0.2513	0.2841	13495	13732
62	3884	3400	0.2543	0.2872	13524	13761
63	3934	3450	0.2574	0.2902	13555	13793
64	3983.9	3499.9	0.2603	0.2931	13590	13829
65	4033.9	3549.9	0.2632	0.296	13626	13867
66	4083.9	3599.9	0.266	0.2989	13664	13907
67	4133.9	3649.9	0.2687	0.3016	13708	13955
68	4183.9	3699.9	0.2715	0.3044	13746	13996
69	4233.9	3749.9	0.2741	0.307	13790	14046
70	4283.9	3799.9	0.2769	0.3098	13829	14088
71	4333.9	3849.9	0.2794	0.3123	13877	14142
72	4384	3900	0.2819	0.3148	13925	14198

73	4434	3950	0.2844	0.3173	13973	14253
74	4484	4000	0.287	0.3199	14019	14305
75	4534	4050	0.2894	0.3223	14066	14358
76	4584	4100	0.2919	0.3248	14111	14410
77	4634	4150	0.2943	0.3272	14162	14470
78	4684	4200	0.2968	0.3297	14207	14521
79	4734	4250	0.2991	0.332	14258	14581
80	4784	4300	0.3015	0.3344	14306	14637
81	4834	4350	0.3039	0.3368	14353	14691
82	4884	4400	0.3063	0.3392	14399	14743
83	4934	4450	0.3087	0.3417	14441	14791
84	4984	4500	0.3112	0.3441	14484	14839
85	5034	4550	0.3136	0.3466	14526	14885
86	5084	4600	0.316	0.3489	14570	14935
87	5134	4650	0.3183	0.3512	14618	14991
88	5184	4700	0.3206	0.3535	14663	15044
89	5234	4750	0.3229	0.3559	14708	15094
90	5284	4800	0.3253	0.3582	14750	15142
91	5334	4850	0.3276	0.3606	14793	15191